Siemes, H., Klingenberg, B., Rybacki, E., Naumann, M., Schäfer, W., Jansen, E., Kunze, K. (2008): Glide systems of hematite single crystals in deformation experiments. - Ore Geology Reviews, 33, 3-4, 255-279

DOI: 10.1016/j.oregeorev.2006.03.007

Glide systems of hematite single crystals in deformation experiments

H. Siemes[a*], B. Klingenberg[a], E. Rybacki[b], M. Naumann[b], W. Schäfer[c], E. Jansen[c], K. Kunze[d]

[a] Institut für Mineralogie und Lagerstättenlehre, RWTH Aachen, D-52056 Aachen, Germany;
[b] Geoforschungszentrum Potsdam, Telegrafenberg, D-14473 Potsdam, Germany;
[c] Mineralogisches Institut Bonn, Forschungszentrum Jülich, D-52425 Jülich, Germany;
[d] Geologisches Institut ETH Zürich, CH-8092 Zürich, Switzerland

Accepted for publication in "Ore Geology Reviews" since March 2006

Abstract

The critical resolved shear stresses (CRSSs) of hematite crystals were determined in compression tests for *r*-twinning, *c*-twinning and {*a*}<*m*>-slip in the temperature range 25°C to 400°C, at 400 MPa confining pressure, and a strain rate of $10^{-5}s^{-1}$ by Hennig-Michaeli and Siemes, 1982. In the present contribution newly performed experiments on hematite single crystals at temperatures up to 800°C at strain rates of 10^{-5} s^{-1} and 300 MPa confining pressure extends the knowledge about the CRSS of twin and slip modes. Optical observations, neutron diffraction goniometry, SEM forescatter electron images and electron backscatter diffraction are applied in order to identify the glide modes. Both twinning systems and {*a*}<*m*>-slip were confirmed by these methods. Besides the known glide systems the existence of the (*c*)<*a*>-slip system could be stated. Mechanical data establish that the CRSS of *r*-twinning decreases from 140 MPa at 25°C to ~5 MPa at 800°C and for {*a*}<*m*>-slip from >560 MPa at 25°C to ~40 MPa at 700°C. At room temperature the CRSS for *c*-twinning is around 90 MPa and at 600°C ~60 MPa. The data indicate that the CRSSs above 200°C seem to be between the values for *r*-twinning and {*a*}<*m*>-slip. For (*c*)<*a*>-slip only the CRSS at 600°C could be evaluated to ~60 MPa. Exact values are difficult to determine because other glide systems are always simultaneously activated.

Keywords: hematite single crystals, experimental deformation, slip modes, twinning modes, critical resolved shear stresses, polarized light microscopy, infrared microscopy, neutron diffraction goniometry, electron backscatter diffraction

* Corresponding author.
Tel.: +49 241 8095858; fax: +49 241 8092153
E-mail address: siemes@rwth-aachen.de

1. Introduction

The knowledge of the glide modes of hematite is important for the interpretation of textures of experimentally deformed hematite ores, e.g Siemes et al. (2002) and Siemes et al. (2005) and textures of metamorphic hematite ores, see e.g. Hennig-Michaeli (1977), Rosière et al. (2001), and Bascou et al. (2002).

Hematite Fe_2O_3 is a trigonal mineral with corundum structure and a hexagonal cell with dimensions a_0 = 0.5038 nm, c_0 = 1.3772 nm (Blake et al., 1966; Finger and Hazen, 1980) to which refer the symbols for planes (hkil), sets of symmetry related planes {hkil}, directions [uvtw] and sets of symmetry related directions <uvtw>. The melting temperature is 1572±5°C at 5.3 MPa O_2 pressure (Crouch et al. 1971).

The basal and rhombohedral twinning laws of hematite crystals determined by Veit (1922) were confirmed and extended by deformation experiments (Hennig-Michaeli and Siemes, 1982) using a fluid high-pressure high-temperature (HTP) equipment. Displacement and load to be corrected for high friction were measured externally. Low strength aluminum jackets separated the specimens from the confining pressure medium silicon oil. The tests were performed in the temperature range 25°C to 400°C, at 400 MPa confining pressure, and a strain rate of ~$10^{-5}s^{-1}$. Critical resolved shear stresses (CRSSs) were determined for *r*-twinning, *c*-twinning and {*a*}<*m*>-slip.

New results from compression experiments on polycrystalline hematite ores by means of an HTP Paterson gas apparatus were described recently (Siemes et al., 2003). The analysis of the acquired crystallographic preferred orientations measured by means of neutron diffraction indicate that (*c*)<*a*>-slip becomes an increasingly important glide system at temperatures of 600°C and above. Here, we report on a new series of experiments on hematite single crystals, performed under comparable and partially identical conditions to before, in order to verify some of the former results and to identify the active glide systems at even higher temperatures.

2. Experimental methods and starting material

2.1 Starting material and preparation of specimens

Natural hematite single crystals from different locations in Brazil (Fig.1, Table 1) were used as starting material. Tetragonal prismatic specimens $7 \bullet 7 \bullet 14$ mm^3 were prepared in different crystallographic orientations with their top plane either parallel to *c*(0001), *r*$\{01\bar{1}2\}$, *f*$\{10\bar{1}1\}$, *a*$\{11\bar{2}0\}$, or *m*$\{10\bar{1}0\}$, respectively, and two other crystallographically defined side planes (Table 2). Accordingly the specimens are labeled here *c*-crystal, *r*-crystal, etc. Inspection of the undeformed specimens by means of neutron diffraction and light microscopy showed thin *r*-twin lamellae. Some of the *r*-crystals turned out to be growth-twins. They are transferred into each other by a 180° rotation about [0001] or equivalent to a mirror at (0001) with the consequence that the prepared specimens are bi-crystals with varying proportions of *r*$\{01\bar{1}2\}$ and *r*'$\{10\bar{1}2\}$ parallel to the top plane (Fig. 2).

The orientation-(Schmid) factors m (Schmid, 1925; Schmid & Boas, 1935, 1950; Wenk, 1985), which represent the factors between the normal stress σ in compression direction and the resolved shear stress τ parallel to the actual glide plane in glide direction, were calculated

as $\tau = \sigma \bullet \cos\chi \bullet \cos\lambda = \sigma \bullet m$ ($-0.5 \geq m \geq +0.5$), with χ and λ defined as the angles between compression direction and glide direction or normal of the glide plane, respectively. In compression tests glide systems with high positive Schmid factors are preferentially activated. To initiate twinning it is additionally necessary besides positive m-factors that a shortening and not an elongation of the specimen occurs. The data in Table 3 for the known twinning systems and in Table 4 for the known slip systems suggest that c-specimens are most suitable for *r*-twinning and *a*- and *m*-specimens are most suitable for {*a*}<*m*>-slip. The other specimens have medium to high Schmid factors for {*a*}<*m*>-slip, (*c*)<*a*>-slip and *c*-twinning. Table 3 and Table 4 are corrected versions of those originally published by Siemes et al., 2004.

2.2 Deformation apparatus and experimental procedure

The compression tests were performed at the Geoforschungszentrum Potsdam using a high resolution Paterson-type gas-medium apparatus (Paterson, 1970, 1990). Displacement and axial load are internally measured. The sample assembly requires cylindrical specimens with a diameter of 10 mm or 15 mm separated from the confining pressure medium (argon gas) by iron jackets with a wall thickness of 0.34 mm. In order to complement the prismatically shaped single crystals to cylindrical specimens different spacer configurations were tested. Finally, two copper parts with an outer diameter of 15 mm and with inner V-necks fitting the prismatic specimens were used. Silver(70)-palladium(30) foils of 20-40 μm thickness were placed between the specimen and the copper in order to minimize the reaction of hematite with the iron jacket and/or with iron impurities in the copper to form magnetite or wuestite. This arrangement has been successfully used in compression tests on polycrystalline hematite (Siemes et al., 2003).

The data from force-displacement records were corrected for the force sustained by the copper parts and the iron-jacket. For this purpose pure copper specimens with 15 mm diameter and 14 mm length were deformed at the same conditions as for the combined hematite-copper specimens. Stress was calculated assuming constant volume and strain is corrected for the apparatus compliance.

2.3 Neutron diffraction

Complete pole figures representing the crystallographic preferred orientations of the bulk volume were measured with a neutron texture-diffractometer (SV7, Jansen et al., 2000) at the Research Center Juelich. Since this diffractometer is equipped with a position sensitive detector the reflections of *c*(0001), *f*{$10\bar{1}1$}, *r*{$01\bar{1}2$}, *e*{$10\bar{1}4$}, and *a*{$11\bar{2}0$} could be measured in one run over a 2Θ-range of 50° using a wavelength of 0.2332 nm with *c*(0001) obtained from the third order reflection 0003. To detect the very sharp peaks of the single crystals the standard scan grid comprising about 500 sample positions was extended to 14616 positions with a mean distance of 1.5° which needs a measuring time of about three days. The intensity data were corrected for background intensities, normalized, and directly plotted in an equal area projection without interpolation of isolines.

2.4 Polarized light microscopy

After neutron diffraction measurement of the deformed samples, two neighboring sections

were cut parallel to two of the side planes (Table 2) of the deformed prismatic specimens. These were placed side by side in one mould and polished. Using reflected polarized light the visible deformation features were recorded in micrographs.

2.5 Infrared microscopy

Hematite in polished thin sections (~90μm thick) is transparent in infrared light (e.g. Lüders et al., 1999). In IR micrographs *c*- and *r*-twins are visible as well as fluid inclusions (e.g. Rosière & Rios, 2004).

2.6 Electron backscatter diffraction

Crystal orientations were measured locally by means of electron backscatter diffraction (EBSD) on the same sample mounts. The polished sections received a final ultra-fine polish by lapping for several hours using a colloidal silica suspension with a particle size of 25 nm. EBSD measurements (Kunze et al., 1993) were performed on a SEM CamScan CS44LB equipped with an EBSD attachment at ETH-Zürich. Digital images of the diffraction patterns were obtained using a slow-scan-CCD camera (TSL Digiview Flo), which enables on-chip frame integration and background correction. Using the processing software OIM™ version 3.5 (EDAX-TSL Inc.), orientation image microscopy maps (OIM maps) were acquired at a rate of 20 pixels/second. EBSD patterns were recorded using 15 kV accelerating voltage and a beam current of approximately 3nA, with the sample surface tilted by 70°.

Some of the figures in the following chapter 3 contain orientation contrast (OC) images (forescatter electron images showing crystal orientation contrast by grey levels) and colored OIM maps derived from automated EBSD scans over selected parts of the specimen surface. The OIM maps display the EBSD pattern quality parameter by grey levels. Bright pixels relate to sharp diffraction patterns indicating intact crystals and dark levels mean high density of crystal near surface defects, boundaries, obstacles like holes or insufficient surface preparation. Black color is assigned to pixels with non-reliable indexing of the acquired EBSD pattern, defined by a threshold in the confidence index CI<0.1. Twin orientations are highlighted by superimposed color in the maps as well in the adjacent pole figures. All EBSD derived pole figures were rotated into a reference frame with the respective compression axis in the center, so that they are directly comparable to those from neutron diffraction.

3. Experimental results

A total of 20 specimens were deformed up to about 8% at a strain rate of ~$10^{-5}s^{-1}$ and a confining pressure of 300 MPa with the exception of three tests which were run at 400 MPa. The initial intention was to perform tests only at temperatures above 400°C up to 800°C. Due to inconsistencies with former results (CRSS >440 MPa for c-twinning at 400°C and missing tests at 200°C) additional tests were run at 200°C and 400°C. Details of the induced twinning and slip systems and of the mechanical behavior are separately discussed below.

3.1 Slip and twinning modes in the crystals of different orientations

3.1.1 Compression ⊥ (*c*)

In compression tests perpendicular to (*c*) only *r*-twinning is possible (Table 3 and Table 4). For example the specimen H43C1 was deformed 3.4% at 600 ºC and 300 MPa confining pressure. The photos (Fig. 3) of the side planes (*m*) and (*a*) of the prismatic specimen reveal a dense distribution of intersecting traces of *r*-twin lamellae. Optically visible are three intersecting *r*-twin lamellae on the (*m*)-plane and apparently only two on the (*a*)-plane, because two of the three sets on this plane have parallel traces. The corresponding neutron diffraction pole figures of the volume of this specimen (Fig. 4a) show the parent position and three twin positions as interpreted by means of the theoretical pole positions in Fig. 4b. In Fig. 5a the OC image shows three *r*-twins on the side plane (*m*) which are colored (red, blue, green) in the OIM map (Fig. 5b). The pole figures of a section of plane (*m*) in Fig. 5c show the same distribution of poles as the neutron diffraction pole figures (Fig. 4).

3.1.2 Compression $\perp \{a\}$ and $\perp \{m\}$

In compression tests perpendicular to $\{a\}$ or $\{m\}$ only $\{a\}\langle m\rangle$ slip should be activated (Table 3 and Table 4). An example is specimen H42M3, deformed 3.7% at 600 ºC and 300 MPa confining pressure. Macroscopic inspection of the side planes (*a*) and (*c*) of the prismatic specimen revealed no visible deformation elements. But, micrographs show thin *r*-twin lamellae (Figs. 6a and 6b) which may be growth twins or relaxation twins as described in the next section. The corresponding neutron diffraction pole figures of the volume of this specimen (Fig. 7a) show the parent position and, very weakly, two of the three twin positions colored green and blue in the theoretical pole figures in Fig. 7b. In Fig. 8a the OC image shows two *r*-twins on the side plane (*a*) which are colored (red, green) in the OIM map (Fig. 8b), and a secondary *r*-twin (blue) within the red *r*-twin lamellae. The pole figures of a section of side plane (*a*) show additionally the poles of the red (and blue) *r*-twin lamellae (Fig. 8c) which are not detectable in the related neutron diffraction pole figures in Fig. 7.

3.1.3 Compression $\perp\{r\}$ and $\perp\{r'\}$

Bi-crystal specimens with the compression axis perpendicular to $\{r\},\{r'\}$ are in an appropriate orientation for *c*-twinning, but $(c)\langle a\rangle$-slip and $\{a\}\langle m\rangle$-slip are also in a favorable orientation with rather high Schmid factors (Table 4). Several examples with different deformation features are now discussed. Specimen H34R2, representing a bi-crystal, was deformed to 0.7% strain at 200ºC temperature and 400 MPa confining pressure. A composite photomicrograph of the side plane (*a*) is shown in Fig. 9a. The upper part is oriented with $r\{01\bar{1}2\}$ perpendicular to the compression axis and the lower part with $r'\{10\bar{1}2\}$, respectively. The straight boundary between both parts becomes visible because of the differently oriented *r*-twin lamellae. The lower part shows the traces of two collateral twin lamellae with positive Schmid factors of m=0.15. But, in the upper part all three *r*-twins have zero or negative Schmid factors (Table 3). In deformation experiments on corundum with similar orientation also *r*-twin lamellae were observed (Castaing et al., 2004, p. 1122). Their interpretation is that these lamellae are formed by stress relaxation during unloading at the end of the experiments. The twin boundary of the two parts is marked by a straight red line which is parallel to the trace of the prism planes respectively parallel to the trace of the *c*-axis. Fig. 9b shows a detailed micrograph of the twin boundary indicated by a white rectangle in Fig. 9a. In the upper $\{r\}$-part there are faintly visible deformation *c*-twin lamellae perpendicular to the boundary between both parts and ending there. In the lower part there is another thin twin lamellae parallel to the boundary, presented in Fig. 9c at higher magnification. This twin lamella is a growth *c*-twin with *r*-orientation in the $\{r'\}$-part and contains relaxation *r*-twins with an orientation equal to the upper $\{r\}$-part.

The OIM map in Fig. 10 shows the boundary between both parts with pair-wise occurring *r*-twin lamellae in yellow and light blue in the upper part (grey) and green and dark blue in the lower part (auburn). Another OIM map reveals a *c*-twin (auburn) in the upper part with *r*-twins in green and yellow (Fig. 11). Pole figures of sections of plane (*a*) (Fig. 10 and 11) show in both cases that most of the pole maxima are elongated on circles with a rotation axis parallel to one of the {*m*}-normals. This is compatible with (*c*)<*a*>-slip, but the *a*-slip direction perpendicular to the (*m*)-normal has a Schmid factor m=0.0 (Table 4).

Specimen H32R1 was deformed 6.8% at 600°C and 300 MPa confining pressure in compression perpendicular to $r(01\bar{1}2)$ and $r'(10\bar{1}2)$. The upper part of the bi-crystal is oriented with $r\{01\bar{1}2\}$ perpendicular to the compression axis and the lower part with $r'\{10\bar{1}2\}$, respectively (Fig. 12a). The boundary is marked by a curved red line, which is partly parallel to the trace of the prism planes i.e. parallel to the c-axis. The upper left {*r'*}-part close to the irregular boundary to the {*r*}-part is characterized by undulose extinction parallel to the trace of prism planes and the sole occurrence of *c*-twins in the {*r'*}-part (Fig. 12b). The reason might be a local increase or reorientation of stresses, activating *c*-twinning with a Schmid factor of m=0.23, which is much lower than m=0.45 for c-twinning in the {*r*}-part.

Another interesting deformation feature evolved on the side plane $x(0\bar{1}15)$ of specimen H91R deformed 2.8% at 600 ºC and 300 MPa confining pressure in compression perpendicular to $r(01\bar{1}2)$. The OIM map (Fig. 13a) shows *c*- and *r*-twinning and the corresponding OC image shows additionally small local orientation gradients aligned parallel to two traces of the slip planes for (*a*) <*m*>-slip (Fig. 13b). An OIM map in Fig. 13c shows *r*- and *c*-twins on side plane (*a*); the infrared micrograph in Fig. 13c shows fluid inclusion trails.

3.1.4 Compression ⊥{*f*}

Specimens with the compression axis perpendicular to {*f*} are predicted to deform similar to the {*r'*} specimens, i.e. (*c*)<*a*>-slip and {*a*}<*m*>-slip are in a favorable orientation with medium Schmid factors (Table 4), *c*-twinning is rather unlikely and *r*-twinning should be impossible because one system has a high negative Schmid factor and for the other two systems m is zero (Table 3). An example is specimen H93F1, deformed 3.7% at 600 ºC and 300 MPa confining pressure. This is one of the two preliminary tests with specimens which were complemented with aluminum parts to cylinders of 10 mm diameter. At the prism edges hematite is in contact with the iron jacket which causes strong reaction to magnetite (bottom of Fig. 14a). A remarkable amount of *r*-twins with a complicated relationship is visible in Fig. 14. The parent crystal (colored grey in Fig. 14b and black in Fig. 14c) contains broad *r*-twin lamellae (red) and smaller *r*-twin lamellae (green), which are both growth r-twins. The broad *r*-twin lamellae are in a favorable orientation for *r*-twinning because the compression axis is approximately perpendicular to (0001) of these *r*-twins. Therefore, secondary *r*-twins were activated, colored blue in Fig. 14b and blue and auburn in Fig. 14c. However, the auburn poles are hardly detectable in the OIM map in Fig. 14b (small parts inside the red domains).

3.2 Summary of microstructural observations

Table 5 gives an overview of the slip and twinning modes detected in the 20 deformed single crystals by means of microscopy, neutron diffraction and EBSD measurements.

r-twins $K_1\{\bar{1}012\}$ $N_1<\bar{1}01\bar{1}>$ (Table 3) are found at all temperatures in crystals of all orientations. Therefore, *r*-twinning is easily activated. The occurrence of *r*-twins with zero or

negative Schmid factors is attributed, by analogy with corundum, to stress relaxation at the end of the experiments during the unloading process.

c-twins $K_1(0001)$ $N_1<10\bar{1}0>$ (Table 3) are usually detected only in crystals that were deformed up to 600°C in compression perpendicular to $r\{01\bar{1}2\}$. The number of twin lamellae decreases with increasing temperature. Since we did not deform *r*-crystals above 600°C it remains unknown if *c*-twins develop at higher temperature.

$\{a\}<m>$-slip (Table 4) is found in specimens of different orientations at all temperatures. The slip system was proposed by Hennig-Michaeli & Siemes (1982) based on microscopic observations of slip lines on the pre-polished surfaces of deformed specimens. The present indications of this slip mode are found in OC images as small local orientation gradients aligned parallel to the traces of the slip planes. Undulose extinction appears to be caused by $\{a\}<m>$-slip in one specimen.

$(c)<a>$-slip (Table 4) is found in specimens with the compression axis perpendicular to $r\{01\bar{1}2\}$ at all temperatures, provided that the elongation of pole maxima on circles within the EBSD-pole figures is caused by a rotation around an axis parallel to one of the $\{m\}$-normals. However, in most cases the *a*-slip direction perpendicular to the (m)-normal has a Schmid factor m=0.0.

4. Stress-strain curves and critical resolved shear stresses

All measured stress-strain curves are plotted in Figure 15 (left column) together with enlarged sections between 0% up to 1% strain in the right column.

4.1 Stress-strain curves and yield stress

At temperatures below 800°C the samples show strain hardening behavior within the investigated strain range. In order to calculate the critical resolved shear stress for the identified twinning and slip-modes we determined the characteristic points for yield stresses, i.e. the onset of a non-linear increase in stress for each sample, indicated by circles in Figure 15. The yield stress for the onset of secondary slip- and twinning modes at higher stress are usually given by kinks (sharp changes in slope) of the stress-strain curves. Multiplication of the yield stresses with the Schmid factors given in Tables 3 and Table 4 for the inferred slip and twin systems yield an estimate of the associated critical resolves shear stresses.

4.1.1 Compression $\perp$ (c)

The stress-strain curves in Fig. 15a show the four tests at 200°C, 600°C and 700°C. Strength and critical resolved shear stresses for *r*-twinning decrease with increasing temperature.

4.1.2 Compression $\perp$ $\{a\}$ and $\perp$ $\{m\}$

For the stress-strain curves at 600°C in compression tests perpendicular to $\{a\}$ and $\{m\}$ (Fig. 15b and 15c) is characteristic that after reaching a stress maximum the stress decreases and then slowly increases. Before achieving the maximum the curves depart from a linear increase. These points are considered as beginning of $\{a\}<m>$-slip, the only deformation mode with high Schmid factors. The changes in slope of the curve at 30 MPa of specimen HP142 in Fig. 15b and at 44 MPa of specimen H42M2 in Fig. 15c could not be assigned to specific deformation modes.

4.1.3 Compression ⊥{*r*} and ⊥{*r'*}

The stress strain curves in Fig. 15d and Fig. 15e present three tests at 200°C and two tests at 400°C on bi-crystals perpendicular to {*r*} and {*r'*}. The characteristic points in the curves with lower stresses are assigned to *r*-twinning in the {*r'*}-part of the crystals and the points with higher stresses to {*a*}<*m*>-slip.

The stress-strain curves of three tests at 600°C are shown in Fig. 15f and 15g. Specimen H91R1 is completely in an orientation with the compression axis perpendicular to {*r*}. The stress-strain curve in Fig. 15f reveals three linear sections. The first deflection was assigned to formation of *c*-twins (CRSS = 132*0.45 = 59 MPa), the second to {*a*}<*m*>-slip (CRSS = 220*0.31 = 68 MPa), and the third to (*c*)<*a*>-slip (CRSS = 264*0.39 = 103 MPa). On the other hand specimen H33R3 has an orientation with the compression axis perpendicular to {*r'*}. As the stress-strain curve reveals there is no (*c*)<*a*>-slip detectable (Fig. 15f) and *r*-twinning with a low critical resolved shear stress (14 MPa) simultaneously generates together with {*a*}<*m*>-slip (CRSS = 69 MPa) a gradual transition from the linear increasing range of the curve to the slightly increasing strain hardening range. The stress-strain curve just touches but does not cross the expected level of (*c*)<*a*>-slip.

In a third test at 600°C on a {*r*}/{*r'*} bi-crystal, a variety of deformation modes was detected by microstructural observations. In the corresponding stress strain curve (Fig. 15g) only the beginning of {*a*}<*m*>-slip is certain at higher stresses. In the low stress region a stress value could be assigned to *r*-twinning in the {*r'*}-part of the crystal or to *c*-twinning, which is possible in both parts of the crystal.

The crystal of the 800°C test is predominantly in an orientation with the compression axis perpendicular to {*r'*}. There are two assignments possible, one for *r*-twinning and one for {*a*}<*m*>-slip (Fig. 15g).

4.1.4 Compression ⊥{*f*}

Two tests at 700°C and one test at 600°C (Fig. 15h) reveal critical resolved shear stresses between 41 and 44 MPa for {*a*}<*m*>-slip. The kink at a stress of 40 MPa in the 600°C-curve indicates the onset of the secondary r-twinning within the r-growth twin lamellae. Because of the growth twins the stress strain curve reveals a much stronger strain hardening in comparison to the curves of the 700°C tests.

4.2 Critical resolved shear stresses

All determined critical resolved shear stresses for twin- and slip-modes, together with the low temperature data measured by Henning-Michaeli and Siemes (1982), are compiled in Table 6 and plotted in Fig. 16, respectively. The data points are labelled according to the orientation of the compression axis and to their origin (1982 = Hennig-Michaeli and Siemes, 2005 = this study). The data points of {*a*}<*m*>-slip and *r*-twinning are rather widely scattered around two different straight lines in a log10(CRSS) versus temperature plot (compare plots of the deformation modes of corundum crystals e.g. Lagerlöf et al., 1994, Castaing et al., 2004). This is due to the fact that the specimens are from different natural crystals with different properties (e.g. more or less fine distributed growth *r*-twin lamellae) and that tests were run by means of different equipment. Those few tests that were performed with the same conditions using specimens from the same crystal resulted in very similar stress-strain curves and critical resolved shear stresses. The plotted straight lines were fitted by least square calculus and make the dependence on temperature more striking. The CRSS of *r*-twinning decreases from 140 MPa at 25°C to ~5 MPa at 800°C and for {*a*}<*m*>-slip from >560 MPa at room temperature to ~30 MPa at 800°C. For *c*-twinning the CRSS is around 90 MPa (1982) at

room temperature and ~60 MPa at 600°C. The very high value at 400°C (1982) is considered an erroneous estimation. Besides this, *c*-twinning was confirmed by microscopy and EBSD-measurements at all temperatures up to 600°C. A grey dashed line indicates that most probably the CRSS for c-twinning decreases slightly with increasing temperature; above 200°C it is higher than the CRSS of *r*-twinning. For (*c*)<*a*>-slip only one reliable data point at 600°C was determined. But, in local pole figures from EBSD-measurements and inverse pole figures of local misorientations, we found indications of (*c*)<*a*>-slip also at lower temperatures.

5. Outlook

It is intended to investigate the dislocation structure of the deformed hematite single crystals by means of transmission electron microscopy and to compare the results with the equivalent data for isostructural corundum. Infrared microscopy studies of the same crystals are underway to obtain information about the behavior of fluid inclusions depending on varying temperature and strain.

Orbituary

On February 6th, 2006, our co-author Dr. Wolfgang Schäfer died at the age of 63 years. Wolfgang Schäfer was an outstanding and productive scientist. He was the head of the neutron diffraction group at the Mineralogical Institute of the University of Bonn, which was located at the Forschungszentrum Jülich for more than thirty years. During these years he had brought to perfection powder diffractometry and texture analysis by neutrons. In co-operation with external users from various fields of science, e.g. chemistry, physics, materials science and geoscience, a large number of scientific objectives were solved and published. We lost an excellent scientist and a sincere friend.

Acknowledgements

The support by the DFG is gratefully acknowledged. V. Lüders is thanked for the infrared measurement on two of the deformed hematite specimens. Constructive comments of the reviewers A. P. Boyle and L. Lagoeiro are greatly appreciated. BK received a stipend from the ETH student exchange office and thanks for hospitality during a three month stay at ETH Zürich in summer 2003. The staffs of the Mineralogical Institute of the RWTH Aachen, the Geological Institute of the ETH Zürich, the Department Rheology and Tectonophysics of the GFZ Potsdam, and the Mineralogical Institute Bonn of the FZ Juelich contributed with a variety of preparations and measurements.

References

Bascou, J., Raposo, M.I.B., Vauchez, A., Egydio-Silva, M., 2002. Titanohematite lattice-preferred orientation and magnetic anisotropy in high-temperature mylonites. Earth and Planetary Science Letters 198, 77-92.

Blake, R.L., Hessevick, R.E., Zoltai, T., Finger, L.W., 1966. Refinement of the hematite structure. American Mineralogist, 51, 123-129.

Castaing, J., He, A., Lagerlöf, K.P.D. and Heuer, A.H., 2004. Deformation of sapphire (α-Al_2O_3) by basal slip and basal twinning below 700°C. Philosophical Magazine 84, 1113-1125.

Crouch, A.G., Hay, K.A., Pascoe, R.T., 1971. Magnetite-haematite-liquid equilibrium conditions at oxygen pressures up to 53 bar. Nature, Physical Sciences, 234, 132-133.

Finger, L.W., Hazen R.M., 1980. Crystal structure and isothermal compression of Fe2O3, Cr_2O_3, and V_2O_3 to 50 kbars. Journal of Applied Physics 51, 5362-5367.

Hennig-Michaeli, Ch., 1977. Microscopic structure studies of experimentally and naturally deformed hematite ores. Tectonophysics 39, 255-271.

Hennig-Michaeli, Ch. and Siemes, H., 1982. Experimental deformation of hematite crystals between 25°C and 400°C at 400 MPa confining pressure. In: Schreyer, W. (Editor) High Pressure Research in Geoscience, Schweizerbart'sche Verlagsbuchhandlung, Stuttgart, 133-150.

Jansen, E., Schäfer, W., Kirfel, A., 2000. The Jülich neutron diffractometer and data processing in rock texture investigations. Journal of Structural Geology 22, 1559-1564.

Kunze, K., Wright, S.I., Adams B.L. and Dingley D.J., 1993. Advances in automatic EBSD single orientation measurements. Textures and Microstructures 20, 41-54.

Lagerlöf, K.P.D., Heuer, A.H.,Castaing, J., Rivière, J.P, Mitchell, T.E., 1994. Slip and twinning in sapphire (α-Al_2O_3). Journal of the American Ceramic Society, 77, 385-397 .

Lüders, V., Gutzmer,J., Beukes, N.J. 1999. Fluid inclusion studies in cogenetic hematite, hausmannite, and gangue minerals from high-grade manganese ore in the Kalahari Manganese Field, South Africa. Economic Geology 94, 589-596.

Paterson, M.S., 1970. A high pressure, high-temperature apparatus for rock deformation. International Journal of Rock Mechanics and Mining Sciences 7, 517-526.

Paterson M.S., 1990. Rock deformation experimentation. In: Duba, A.G., Durham, W.B., Handin, J.W., Wang H.F. (Editors), The Brittle-Ductile Transition in Rocks. The Heard Volume, American Geophysical Union Geophysical Monograph 56, 187-194.

Rosière, C.A., Rios, F.J., 2004. The origin of hematite in high grade ores based on microscopy and fluid inclusion studies: the example of the Conceiçao Mine, Quadrilátero Ferrífero, Brazil. Economic Geology 99, 611-624.

Rosière, C.A., Siemes, H., Quade, H., Brokmeier, H.-G., Jansen, E.M., 2001. Microstructures, textures and deformation mechanism in hematite. Journal of Structural Geology 23, 1429-1440.

Schmid, E., 1925: Neuere Untersuchungen an Metallkristallen. In: Biezeno, C.B., Burgers, J.M. (Editors), Proceedings of the First International Congress for Applied Mechanics, Delft 1924, Technische Boekhandel en Drukkerij J. Waltman Jr., Delft, 342-353.

Schmid, E., Boas, W., 1935. Kristallplastizität. Springer, Berlin; (english translation, Plasticity of Crystals. F. A. Hughes & Co., London, 1950).

Siemes, H., Klingenberg, B., Rybacki., E., Naumann, M., Schäfer, W., Jansen, E., Rosière, C.A., 2003. Texture, microstructure, and strength of hematite ores experimentally deformed in the temperature range 600-1100°C and at strain rates between 10^{-4} and 10^{-6} s^{-1}. Journal of Structural Geology 25, 1371-1391.

Siemes, H., Klingenberg, B., Rybacki, E., Naumann, M., Schäfer, W., Jansen, E., Kunze, K., 2004. Glide systems of hematite single crystals in deformation experiments. In: Pecchio,

M., Andrade, F.R.D., D'Agostino, L.Z. , Kahn, H., Sant'Agostino, L.M., Tassinari, M.M.M.L. (Editors), Applied Mineralogy: Development in Sciences and Technology, São Paulo, ICAM2004, vol. 2, 947-949.

Siemes, H., Klingenberg, B., Rybacki, E., Naumann, M., Walter, J.M., Jansen, E., Kunze, K., 2005. Microstructure and texture of hematite ore deformed to large strain in torsion. Berichte der Deutschen Mineralogischen Gesellschaft, Beihefte European Journal of Mineralogy 17, 129.

Veit, K., 1922. Künstliche Schiebungen und Translationen in Mineralien. Neues Jahrbuch für Mineralogie, Geologie und Paläontologie, Beilage-Band 45, 121-148.

Wenk, H.R. Editor, 1985. Preferred orientation in deformed metals and rocks: An introduction to modern texture analysis. Academic Press, Orlando.

Table 1
Single crystals of hematite used in deformation experiments *)

crystal	location in Brazil	size of crystal mm • mm • mm	macroscopically identifiable crystal faces
H 1	Santa Ana dos Ferros, Ouro Preto	53 • 52 • 21	*r* $\{01\bar{1}2\}$: trig. rhombohedron
H 2	Dom Bosco, Minas Gerais	55 • 40 • 35	*e* $\{10\bar{1}4\}$: trig. rhombohedron
H 3	Minas Gerais	47 • 43 • 40	*n* $\{11\bar{2}3\}$: hex. dipyramid
H 4	Minas Gerais	38 • 37 • 30	*c* (0001): basal pinacoid
H 5	Serra dos Cristais, Goiás	42 • 29 • 29	*r*-twin lamellae
H 9	Minas Gerais	46 • 23 • 19	

*) H1, H2 in Hennig-Michaeli & Siemes, 1982; H3, H4, H5, H9 this study

Table 2
Crystallography of the prismatic specimens *)

top plane	side plane 1	side plane 2
c (0001)	*a*(11$\bar{2}$0)	*m*(10$\bar{1}$0)
r (01$\bar{1}$2)	*a*(11$\bar{2}$0)	*x*(01$\bar{1}$5)
r'(10$\bar{1}$2)	*a*(11$\bar{2}$0)	*x*'(10$\bar{1}$5)
a(11$\bar{2}$0)	*m*(10$\bar{1}$0)	*c* (0001)
m(10$\bar{1}$0)	*a*(11$\bar{2}$0)	*c* (0001)
f(10$\bar{1}$1)	*a*(11$\bar{2}$0)	($\bar{1}$.0.1.10)

*) Deviation from the indicated {hkil} plane approximately up to ± 2°

Table 3
Hematite twin modes

r-twins	*c*-twins
1:K_1=($\bar{1}$012) N_1=[$\bar{1}$01$\bar{1}$]	4:K_1=(0001) N_1=[10$\bar{1}$0]
2:K_1=(1$\bar{1}$02) N_1=[1$\bar{1}$0$\bar{1}$]	5:K_1=(0001) N_1=[$\bar{1}$100]
3:K_1=(01$\bar{1}$2) N_1=[01$\bar{1}\bar{1}$]	6:K_1=(0001) N_1=[0$\bar{1}$10]

Schmid factors m and strain by twinning ε [in %] in uniaxial compression for various crystal orientations relative to principal stress direction σ_1

r-twins

$\sigma_1 \perp$ to	m_1	m_2	m_3	ε_1	ε_2	ε_3
c (0001)	0.45	0.45	0.45	9.1	9.1	9.1
r (01$\bar{1}$2)	0.00	-0.05	-0.05	-2.1	-1.0	-1.0
r'(10$\bar{1}$2)	-0.38	0.15	0.15	-8.0	2.1	2.1
f (10$\bar{1}$1)	-0.49	0.00	0.00	-10.5	-0.7	-0.7
a (11$\bar{2}$0)	-0.34	-0.34	0.00	-7.8	-7.8	0.0
m (10$\bar{1}$0)	-0.45	-0.11	-0.11	-10.3	-2.7	-2.7

c-twins

$\sigma_1 \perp$ to	m_4	m_5	m_6	ε_4	ε_5	ε_6
c (0001)	0.00	0.00	0.00	-18.4	-18.4	-18.4
r (01$\bar{1}$2)	0.45	-0.23	-0.23	26.4	-18.4	-18.4
r'(10$\bar{1}$2)	-0.45	0.23	0.23	-30.0	9.0	9.0
f (10$\bar{1}$1)	-0.29	0.14	0.14	-18.4	7.6	7.6
a (11$\bar{2}$0)	0.00	0.00	0.00	0.0	0.0	0.0
m (10$\bar{1}$0)	0.00	0.00	0.00	0.0	0.0	0.0

Table 4
Hematite slip modes

(*c*)<*a*>-slip	{*a*}<*m*>-slip
7:*c*(0001) *a*[2$\bar{1}\bar{1}$0]/[$\bar{2}$110]	10:*a*(2$\bar{1}\bar{1}$0) *m*[0$\bar{1}$10]/[01$\bar{1}$0]
8:*c*(0001) *a*[$\bar{1}$2$\bar{1}$0]/[1$\bar{2}$10]	11:*a*($\bar{1}$2$\bar{1}$0) *m*[10$\bar{1}$0]/[$\bar{1}$010]
9:*c*(0001) *a*[$\bar{1}\bar{1}$20]/[11$\bar{2}$0]	12:*a*($\bar{1}\bar{1}$20) *m*[$\bar{1}$100]/[1$\bar{1}$00]

Schmid factors m in uniaxial compression for various crystal orientations relative to principal stress direction σ_1

$\sigma_1 \perp$ to	m_7	m_8	m_9	m_{10}	m_{11}	m_{12}
c (0001)	0.00	0.00	0.00	0.00	0.00	0.00
r (01$\bar{1}$2)	0.39	0.00	0.39	0.31	0.00	0.31
r'(10$\bar{1}$2)	0.39	0.00	0.39	0.31	0.00	0.31
f (10$\bar{1}$1)	0.25	0.00	0.25	0.39	0.00	0.39
a (11$\bar{2}$0)	0.00	0.00	0.00	0.00	0.43	0.43
m (10$\bar{1}$0)	0.00	0.00	0.00	0.43	0.00	0.43

Table 5
Slip- and twinning modes in deformed hematite single crystals identified by microscopy, neutron diffraction and EBSD measurements

compression axis ⊥	tempera-ture °C	*r*-twinning	*c*-twinning ⊥{*r*}	*c*-twinning ⊥{*r'*}	{*a*}<*m*>-slip	(*c*)<*a*>-slip
(*c*)	200	H52C1				
(*c*)	600	H43C1				H43C1 misorien[4])
(*c*)	700	H43C3,H92C				
{*a*}	600	HP142			HP142	
{*a*}		HS230			HS230 slip[2])	
{*m*}	600	H42M3			H42M3	H42M3 misorien
{*m*}	700	H42M2				
{*r*}+{*r'*} 0.1-0.6[1])	200	H33R1,H34R1, H34R2	H33R1,H34R1, H34R2			H34R2 rot<*m*>[5]
{*r*}+{*r'*} 0.9-1.0	400	H32R2,H33R2				H32R2 rot<*m*>
{*r*}+{*r'*} 0.0	600	H91R1	H91R1		H91R1 slip	
{*r*}+{*r'*} 0.5	600	H32R1	H32R1	H32R1	H32R1 undul[3])	H32R1 rot<m>
{*r*}+{*r'*} 1.0	600	H33R3				
{*r*}+{*r'*} 0.9	800	H34R3				H34R3 rot<*m*>
{*f*}	600	H93F1			H93F1 slip	H93F1 misorien
{*f*}	700	H41F1,H41F2				

1) roughly estimated fractions of {*r'*}
2) slip = slip lines = traces of local variation in OC images
3) undul = undulose extinction parallel to traces of prism planes
4) misorien = misorientation maxima in inverse pole figures close to one of the poles of {*m*}
5) rot<*m*> = elongation of pole maxima on circles with a <*m*>-axis ⊥ to an <*a*>-slip direction

Table 6
Compression experiments on hematite crystals, strain rate ~$10^{-5}s^{-1}$

specimen	compression axis ⊥		tempera-ture °C	confining pressure MPa	maximum strength MPa	shortening ε %	glide mode	yield stress MPa	Schmid factor m	CRSS MPa
H1P20*	(*c*)		25	400	714	3.6	*r*-twinning	300	.46	138
H52C1	(*c*)		200	300	807	4.7	*r*-twinning	160	.45	72
H1P41*	(*c*)		400	400	439	5.3	*r*-twinning	45	.48	22
H43C1	(*c*)		600	300	283	3.4	*r*-twinning	72	.45	32
H92C1	(*c*)		700	300	191	3.9	*r*-twinning	34	.45	15
H43C3	(*c*)		700	300	125	1.9	*r*-twinning	34	.45	15
H1P43*	(*a*)		200	400	925	7.8	{*a*}<*m*>-slip	870	.43	374
HP142	(*a*)		600	400	225	4.0	{*a*}<*m*>-slip	160	.43	69
							??	30		
H42M3	(*m*)		600	300	256	3.3	{*a*}<*m*>-slip	176	.43	76
H42M2	(*m*)		700	300	210	3.6	{*a*}<*m*>-slip	100	.43	43
HS230	(*a*)		600	300	257	2.9	{*a*}<*m*>-slip	156	.43	67
							??	44		
	(*r*)	(*r'*)								
H1S22*	1.0		25	400	253	4.9	*c*-twinning	190	.48	91
H34R2	0.5	0.5 **	200	400	1303	0.7	{*a*}<*m*>-slip	1086	.31	337
							r-tw. in *r'*	656	.15	98
H33R1	0.4	0.6 **	200	300	1163	3.6	{*a*}<*m*>-slip	880	.31	273
							r-tw. in *r'*	320	.15	48
H34R1	0.9	0.1 **	200	300	1163	3.4	{a}<m>-slip	880	.31	273
							r-tw. in *r'*	320	.15	48
H32R2		1.0	400	300	775	4.9	{*a*}<*m*>-slip	488	.31	151
							r-tw. in *r'*	288	.15	43
H33R2	0.1	0.9 **	400	300	767	5.0	{*a*}<*m*>-slip	408	.31	126
							r-tw. in *r'*	320	.15	48
H1S21*	1.0		400	400	980	6.7	{*a*}<*m*>-slip	450	.36	162
H91R1	1.0		600	300	396	2.8	*c*-twinning	132	.45	59
							{*a*}<*m*>-slip	220	.31	68
							(*c*)<*a*>-slip	264	.39	103
H32R1	0.5	0.5 **	600	300	324	6.8	{*a*}<*m*>-slip	216	.31	67
							r-tw. in r'	100	.15	15
							c-twinning ?	100	.45	?45
H33R3		1.0	600	300	295	7.7	*r*-tw. in *r'*	92	.15	14
H34R3	0.1	0.9 **	800	300	113	6.7	{*a*}<*m*>-slip	100	.31	31
							r-tw. in *r'*	30	.15	5
H1S12*	(*f*)		25	400	1325	-.-	{*a*}<*m*>-slip	-		>560
H1S11*	(*f*)		400	400	617	5.7	{*a*}<*m*>-slip	450	.39	175
H93F1	(*f*)		600	400	310	3.7	{*a*}<*m*>-slip	112	.39	44
							r-twinning	40	.45	18
H41F1	(*f*)		700	300	257	3.5	{*a*}<*m*>-slip	104	.39	41
H41F2	(*f*)		700	300	303	3.2	{*a*}<*m*>-slip	104	.39	41
H1P51*	(10°*a*)		25	400	570	3.3	*c*-twinning	430	.24	103
H1P52*	(10°*a*)		400	400	490	7.0	{*a*}<*m*>-slip	400	.40	160

*) Hennig-Michaeli and Siemes, 1982, Tab. 4 and Tab. 5
**) roughly estimated fractions

Figure captions

Figure 1
The photo presents one example of the natural hematite crystals (no. 9 in table 1) which were used to prepare the test specimens.

Figure 2.
Specimen H33R1 undeformed bi-crystal prepared for a compression test perpendicular to $r\{01\bar{1}2\}$, pole figures (equal area projection, upper hemisphere) of the $c(0003)$-, $r(01\bar{1}2)$-, $e(10\bar{1}4)$- and $a(11\bar{2}0)$-reflection measured by neutron diffraction: color sequence black, green, magenta, blue, red indicates increasing density, a) measured poles marked with black circles indicate the crystal part with $r\{01\bar{1}2\}$ in the center of the r-pole figure, b) measured poles marked with violet circles indicate the crystal part with $r'\{10\bar{1}2\}$ in *c*-twin position to $r\{01\bar{1}2\}$.

Figure 3.
Specimen H43C1 deformed 3.4% at 600ºC and 300 MPa confining pressure in compression perpendicular to *c*(0001) (compression direction top to bottom of the micrographs), a) optically, three intersecting *r*-twin lamellae are visible on the (*m*)-plane, b) only two *r*-twin lamellae are visible on the (*a*)-plane, because two lamellae have parallel traces.

Figure 4.
Specimen H43C1 deformed 3.4% in compression perpendicular to *c*(0001) at 600ºC and 300 MPa confining pressure (compression direction perpendicular to plane of projection), a) pole figures (equal area projection, upper hemisphere) of the $c(0003)$-, $r(01\bar{1}2)$-, $e(10\bar{1}4)$-and $a(11\bar{2}0)$-reflection measured by neutron diffraction, color sequence: black, green, magenta, blue, red indicates increasing density, b) theoretical pole positions: parent crystal (black), three *r*-twins (red, blue, green).

Figure 5.
Specimen H43C1 deformed 3.4% at 600ºC and 300 MPa confining pressure in compression perpendicular to *c*(0001) (compression direction top to bottom of the micrographs), a) OC image on side plane (*m*), b) OIM map with three *r*-twins (red, blue, green), c) pole figures (equal area projection, upper hemisphere) of plane (*m*) rotated in a position with compression direction perpendicular to the plane of projection: parent crystal (black), three *r*-twins (red, blue, green). The colors in the pole figures correspond to those in the OIM image.

Figure 6.
Specimen H42M3 deformed 3.7% at 600 ºC and 300 MPa confining pressure in compression perpendicular to $m\{10\bar{1}0\}$ (compression direction top to bottom of the micrographs). Micrographs of the side planes (*a*) and (*c*), optically are visible only a few intersecting *r*-twin lamellae on both planes.

Figure 7.
Specimen H42M3 deformed 3.7% at 600 ºC and 300 MPa confining pressure in compression perpendicular to $m\{10\bar{1}0\}$ (compression direction perpendicular to plane of projection), a) pole figures (equal area projection, upper hemisphere) of the $c(0003)$-, $r(01\bar{1}2)$-, $e(10\bar{1}4)$-and $a(11\bar{2}0)$-reflection measured by neutron diffraction, color sequence: black, green, magenta,

blue, red indicates increasing density, b) theoretical pole positions: parent crystal (black), two (blue, green) of the three *r*-twins are detectable.

Figure 8.
Specimen H42M3 deformed 3.7% at 600 ºC and 300 MPa confining pressure in compression perpendicular to $m\{10\bar{1}0\}$ (compression direction top to bottom of the micrographs), a) OC image of side pane (*a*), b) OIM map with two *r*-twins (red, green) and a small secondary *r*-twin within the red twin lamellae, c) pole figures (equal area projection, upper hemisphere) of plane (*a*) rotated in a position with compression direction perpendicular to the plane of projection: parent crystal (black), three *r*-twins (red, blue, green). The colors in the pole figures correspond to those in the OIM image.

Figure 9.
Specimen H34R2 deformed 0.7% at 200 ºC and 400 MPa confining pressure in compression perpendicular to $r(01\bar{1}2)$ and $r'(10\bar{1}2)$ (compression direction top to bottom of the micrographs), a) composite photomicrograph of the side plane (*a*), upper part with the compression perpendicular to {*r*} and lower part perpendicular to {*r*'}, intersecting *r*-twin lamellae are visible optically in different directions according to the schematic figures, b) enlarged section of Fig. 9a with deformation *c*-twin lamella within the {*r*}-part perpendicular to the boundary of both parts and a growth *c*-twin lamella within {*r*'}-part parallel to the boundary, c) enlarged section of Fig. 9b explaining the orientation of the growth *c*-twin by means of the traces of the *r*-twins within the {*r*'}-part of the specimen.

Figure 10.
Specimen H34R2 deformed 0.7% at 200 ºC and 400 MPa confining pressure in compression perpendicular to $r(01\bar{1}2)$ and $r'(10\bar{1}2)$ (compression direction top to bottom of the micrographs), a) OIM map on side plane (*a*) with the boundary between both parts with pairwise occurring *r*-twin lamellae in colors yellow and light blue in the upper part (grey) and green and dark blue in the lower part (auburn) b) pole figures (equal area projection, upper hemisphere) of plane (*a*) rotated in a position with compression direction perpendicular to the plane of projection: parent crystal (*r*) in black with two *r*-twins in yellow and light blue and *c*-twin (*r*') in auburn with two *r*-twins in green and dark blue. The pole maxima are elongated on circles around one of the {*m*}-normals (circled violet) which has acted as a rotation axis. The colors in the pole figures correspond to those in the OIM image.

Figure 11.
Specimen H34R2 deformed 0.7% at 200 ºC and 400 MPa confining pressure in compression perpendicular to $r(01\bar{1}2)$ (compression direction top to bottom of the micrographs), a) OIM map on side plane (*a*) with a *c*-twin in auburn and two *r*-twin lamellae in colors yellow and green b) pole figures (equal area projection, upper hemisphere) of plane (*a*) rotated in a position with compression direction perpendicular to the plane of projection: parent crystal (*r*) in black with two *r*-twins in yellow and green and *c*-twin in auburn. The pole maxima are elongated on circles around one of the {*m*}-normals (circled violet) which has acted as a rotation axis. The colors in the pole figures correspond to those in the OIM image.

Figure 12.
Specimen H32R1 deformed 6.8% at 600 ºC and 300 MPa confining pressure in compression perpendicular to $r(01\bar{1}2)$ and $r'(10\bar{1}2)$ (compression direction top to bottom of the micrographs), a) composite photomicrograph of the side plane (*a*), upper part with the compression perpendicular to {*r*} and lower part perpendicular to {*r*'}, intersecting *r*-twin

lamellae are visible optically in different directions according to the schematic figures within the figure, b) enlarged section of Fig. 12a with undulose extinction parallel to traces of prism planes (*a*) with deformation *c*-twin lamellae perpendicular to the boundary of both parts within the {*r*'}-part.

Figure 13.
Specimen H91R deformed 2.8% at 600 ºC and 300 MPa confining pressure in compression perpendicular to $r(01\bar{1}2)$ (compression direction top to bottom of the micrographs), a) OIM map with *c*-twin and *r*-twin on the side plane x$(0\bar{1}15)$, b) OC image with *c*-twin, *r*-twin, and small local orientation gradients aligned parallel to the traces of the (*a*) <*m*>-slip system on the same place, c) infrared micrograph (by V. Lüders, 2002) and OIM map of side plane $a(11\bar{2}0)$ with similar twins from different locations and with different magnifications, indicated are *c*-twins, *r*-twins and fluid inclusions.

Figure 14.
Specimen H93F1 deformed 3.7% at 600 ºC and 300 MPa confining pressure in compression perpendicular to $f(10\bar{1}1)$ (compression direction top to bottom of the micrographs), a) micrograph on side plane (*a*), white lines indicate the traces of the basal plane, black lines indicate parent crystal, red and green lines indicate traces of *r*-growth twins, blue indicates secondary *r*-twins in the red *r*-growth twins, b) the OIM map shows an enlarged section within micrograph, c) pole figures (equal area projection, upper hemisphere) of the area of the OIM map rotated in a position with compression direction perpendicular to the plane of projection: parent crystal in black with two *r*-growth twins in red and green and two secondary *r*-twins in blue and auburn. The colors in the pole figures correspond to those in the OIM image.

Figure 15.
Stress-strain curves of all 20 deformed hematite single crystals (left column); the assignment of deformation modes and critical resolved shear stresses is shown in appropriately scaled figures of the right column. a) Stress-strain curves of three tests with $\sigma_1 \perp c(0001)$ at temperatures between 200°C and 700°C, b) stress-strain curves of two tests with $\sigma_1 \perp a\{11\bar{2}0\}$ at 600°C, c) stress-strain curves of two tests with $\sigma_1 \perp m\{10\bar{1}0\}$ at 600°C and 700°C, d) stress-strain curves of three tests with $\sigma_1 \perp r\{01\bar{1}2\}/r'\{10\bar{1}2\}$ bi-crystals at 200°C, e) stress-strain curves of two tests with $\sigma_1 \perp r\{01\bar{1}2\}/r'\{10\bar{1}2\}$ bi-crystals at 400°C, f) stress-strain curves of two tests with $\sigma_1 \perp r\{01\bar{1}2\}$ in specimen H91R and $r'\{10\bar{1}2\}$ in specimen H33R3 at 600°C, g) stress-strain curves of two tests with $\sigma_1 \perp r\{01\bar{1}2\}/r'\{10\bar{1}2\}$ bi-crystals at 600°C and 800°C, h) stress-strain curves of one test with $\sigma_1 \perp f\{10\bar{1}1\}$ at 600°C and two tests at 700°C.

Figure 16.
Plot of the log10(CRSS) vs. temperature, data points are labeled according the orientation of the compression axis and to their origin (1982 = Hennig-Michaeli and Siemes, 2005 = this study). Best-fit curves were drawn through the data points of {*a*}<*m*>-slip and *r*-twinning in order to visualize the relationship.

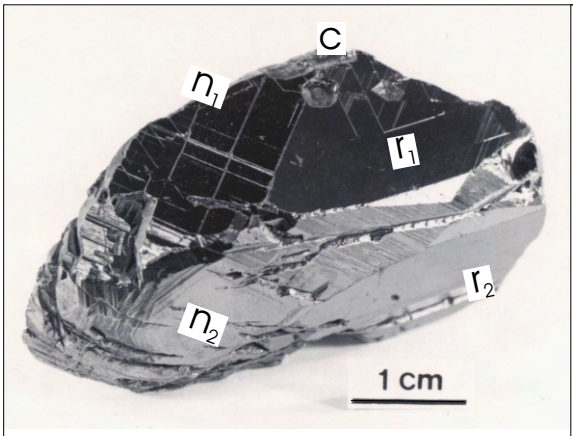

Fig. 1

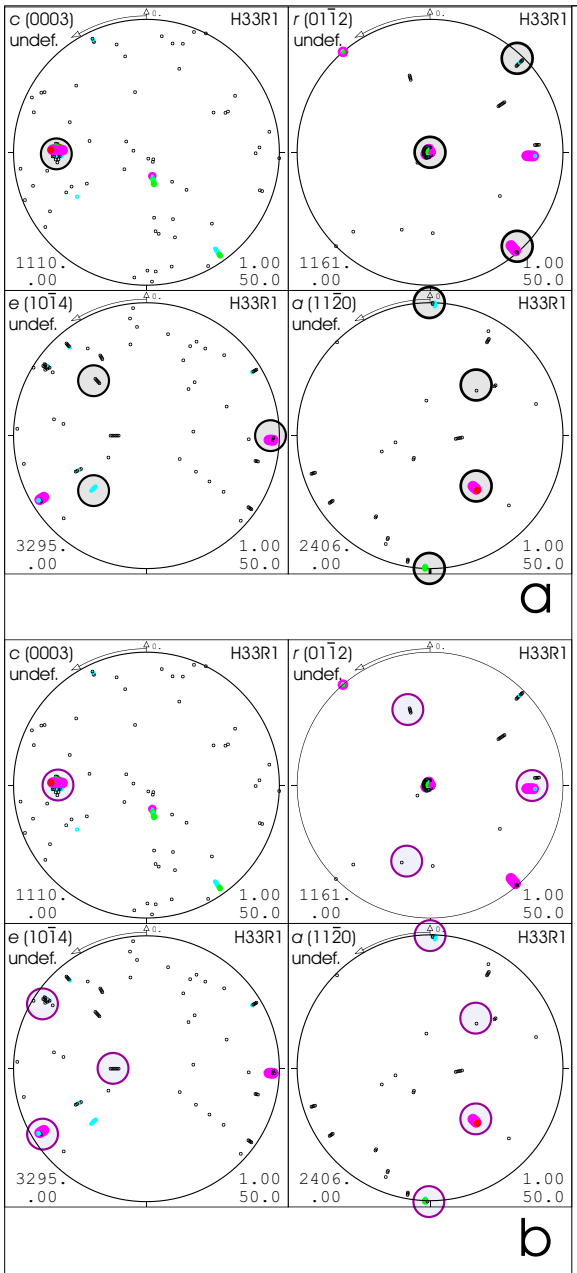
c (0003)
undef.
H33R1
r (01$\bar{1}$2)
undef.
H33R1
1110.
.00
1.00
50.0
1161.
.00
1.00
50.0
e (10$\bar{1}$4)
undef.
H33R1
a (11$\bar{2}$0)
undef.
H33R1
3295.
.00
1.00
50.0
2406.
.00
1.00
50.0
a
c (0003)
undef.
H33R1
r (01$\bar{1}$2)
undef.
H33R1
1110.
.00
1.00
50.0
1161.
.00
1.00
50.0
e (10$\bar{1}$4)
undef.
H33R1
a (11$\bar{2}$0)
undef.
H33R1
3295.
.00
1.00
50.0
2406.
.00
1.00
50.0
b

Fig. 2

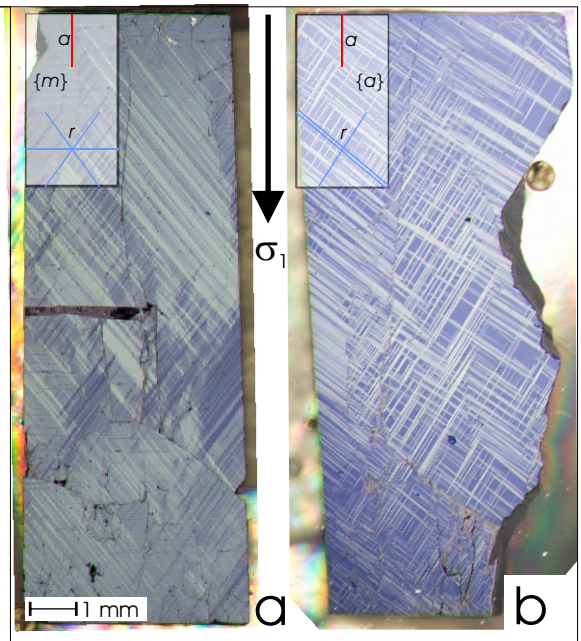
a
{m}
r
σ1
1 mm
a
a
{a}
r
b

Fig. 3

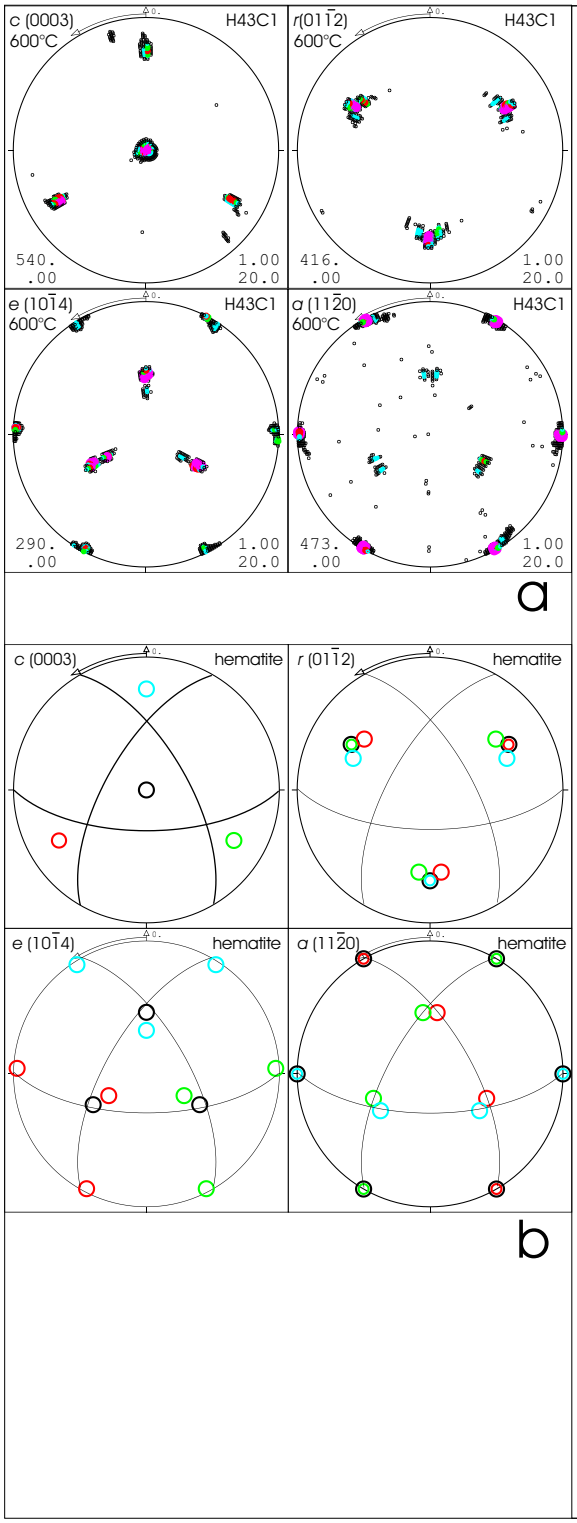
c (0003) 600°C H43C1
r(01$\bar{1}$2) 600°C H43C1
e (10$\bar{1}$4) 600°C H43C1
a (11$\bar{2}$0) 600°C H43C1
540. .00 1.00 20.0
416. .00 1.00 20.0
290. .00 1.00 20.0
473. .00 1.00 20.0
a
c (0003) hematite
r (01$\bar{1}$2) hematite
e (10$\bar{1}$4) hematite
a (11$\bar{2}$0) hematite
b

Fig. 4

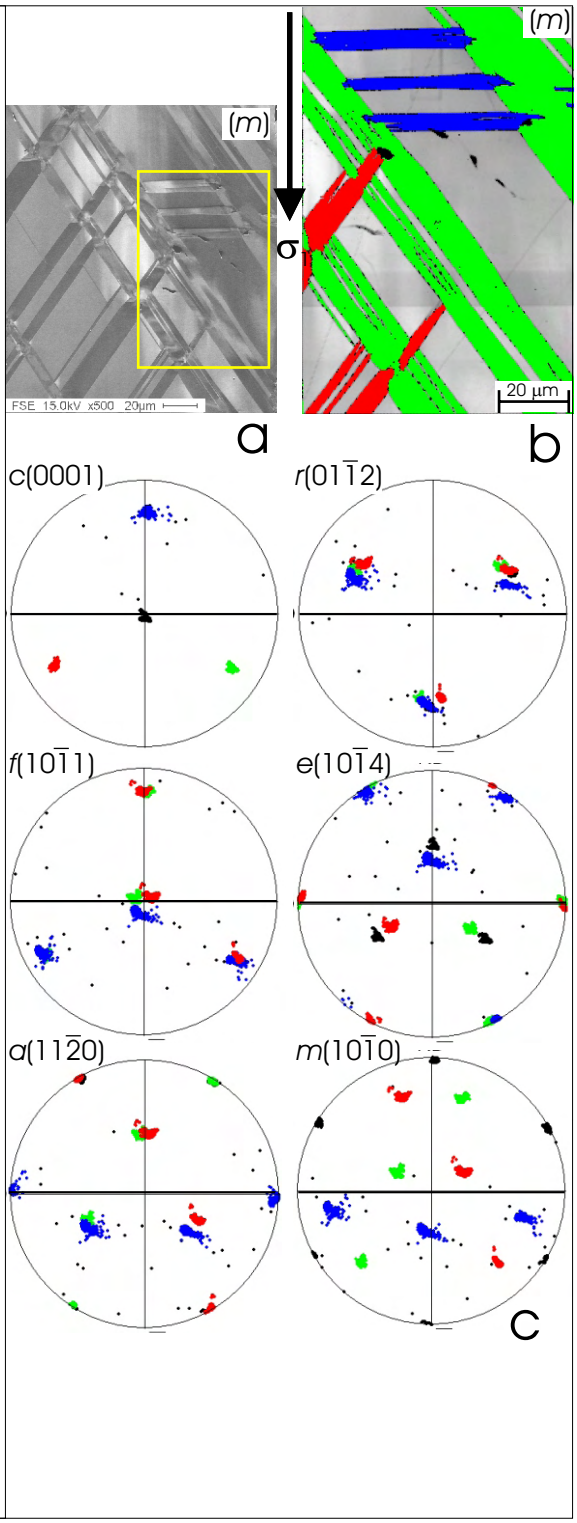
(m)
σ
(m)
FSE 15.0kV x500 20µm
20 µm
a
b
c(0001)
r(01$\bar{1}$2)
f(10$\bar{1}$1)
e(10$\bar{1}$4)
a(11$\bar{2}$0)
m(10$\bar{1}$0)
c

Fig. 5

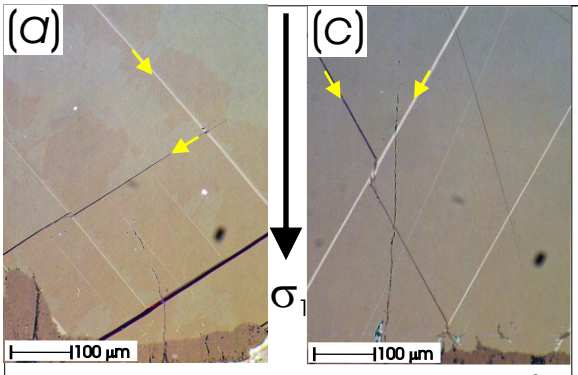
(a)
(c)
σ1
100 µm
100 µm

a b

Fig. 6

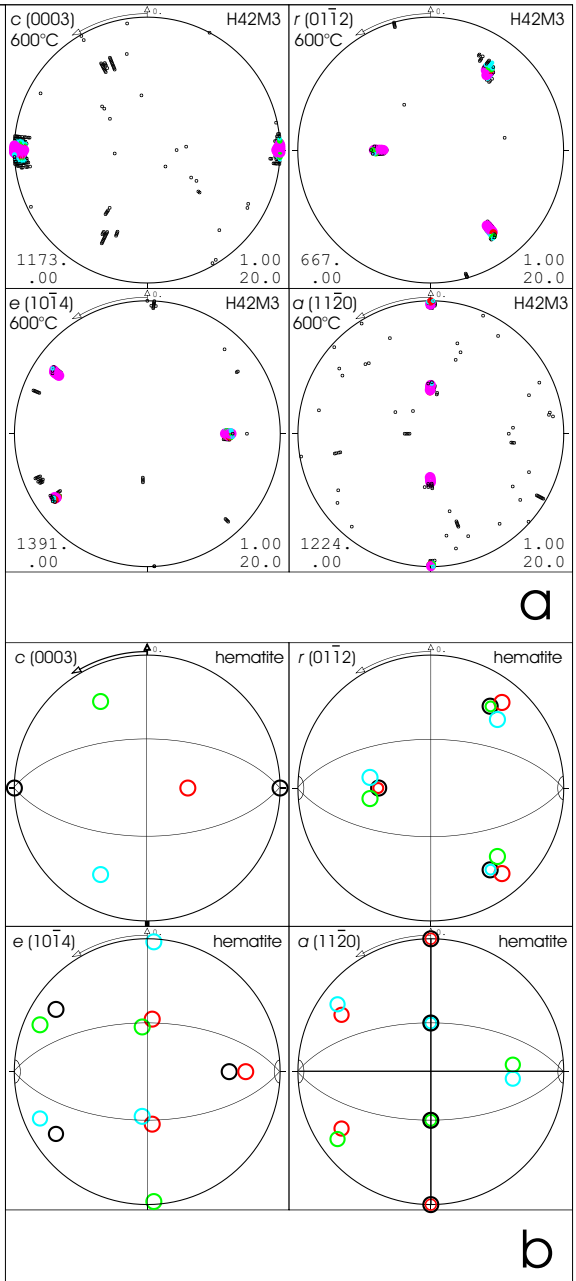
c (0003)
600°C
H42M3
1173.
.00
1.00
20.0
r (01$\bar{1}$2)
600°C
H42M3
667.
.00
1.00
20.0
e (10$\bar{1}$4)
600°C
H42M3
1391.
.00
1.00
20.0
a (11$\bar{2}$0)
600°C
H42M3
1224.
.00
1.00
20.0
a
c (0003)
hematite
r (01$\bar{1}$2)
hematite
e (10$\bar{1}$4)
hematite
a (11$\bar{2}$0)
hematite
b

Fig. 7

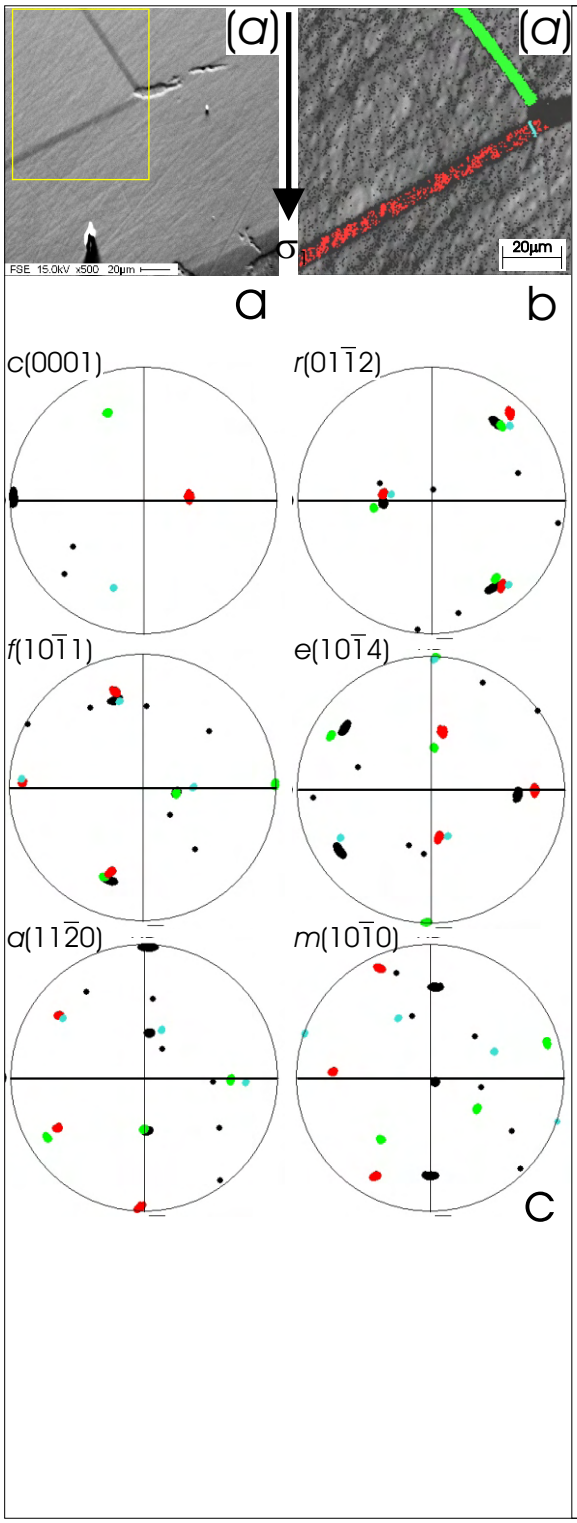
(a)
σ
FSE 15.0kV x500 20µm
(a)
20µm
a
b
c(0001)
r(01$\bar{1}$2)
f(10$\bar{1}$1)
e(10$\bar{1}$4)
a(11$\bar{2}$0)
m(10$\bar{1}$0)
c

Fig. 8

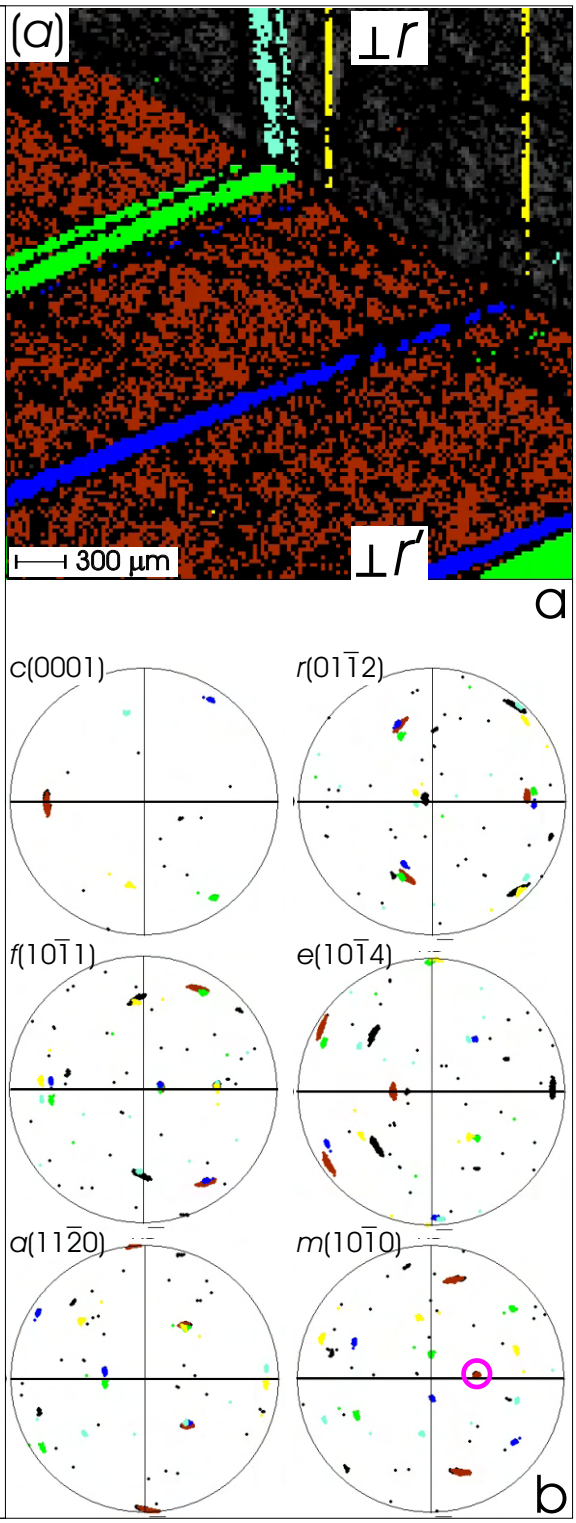
(a)
⊥r
300 µm
⊥r'
a
c(0001)
r(01$\bar{1}$2)
f(10$\bar{1}$1)
e(10$\bar{1}$4)
a(11$\bar{2}$0)
m(10$\bar{1}$0)
b

Fig. 10

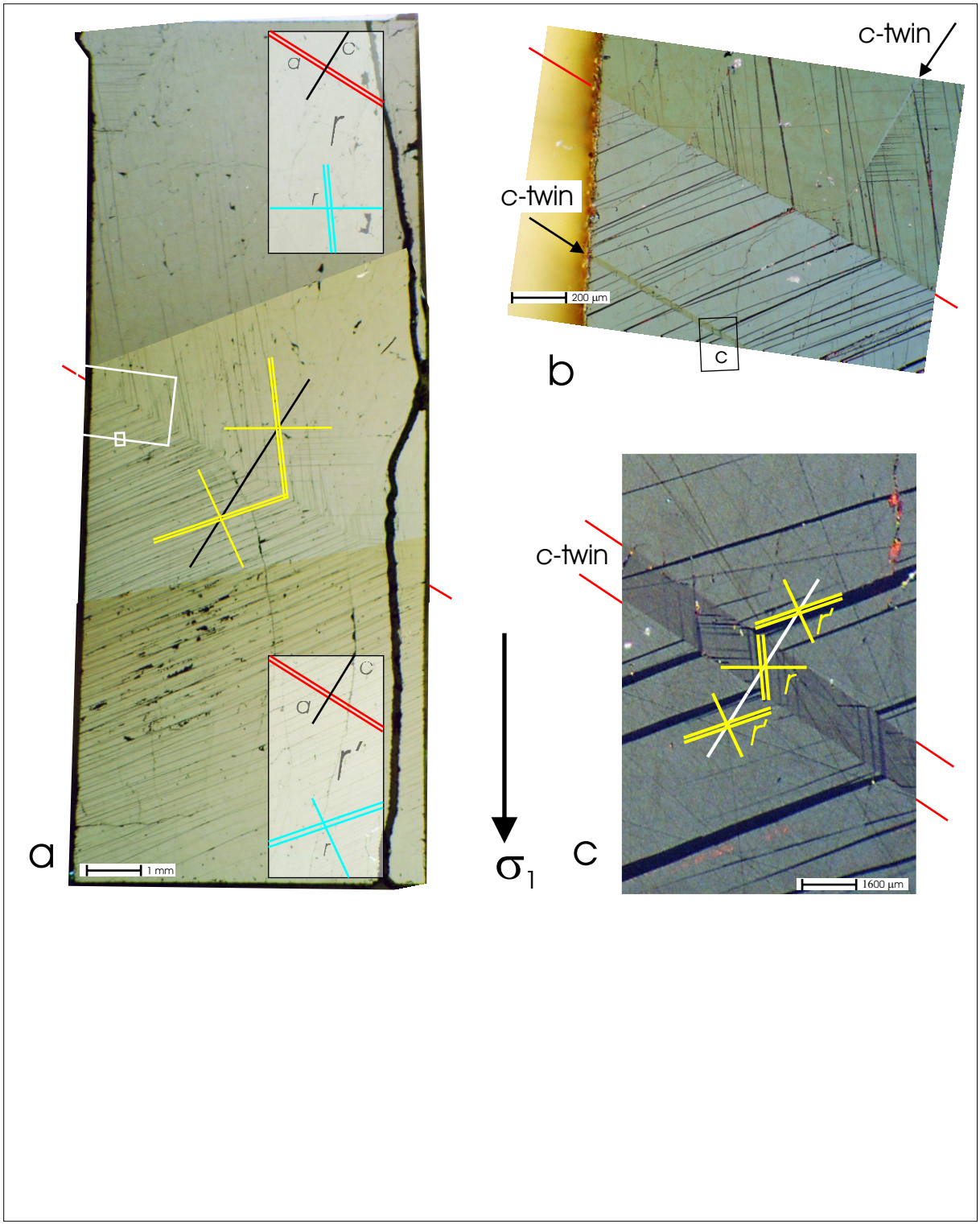

Fig. 9

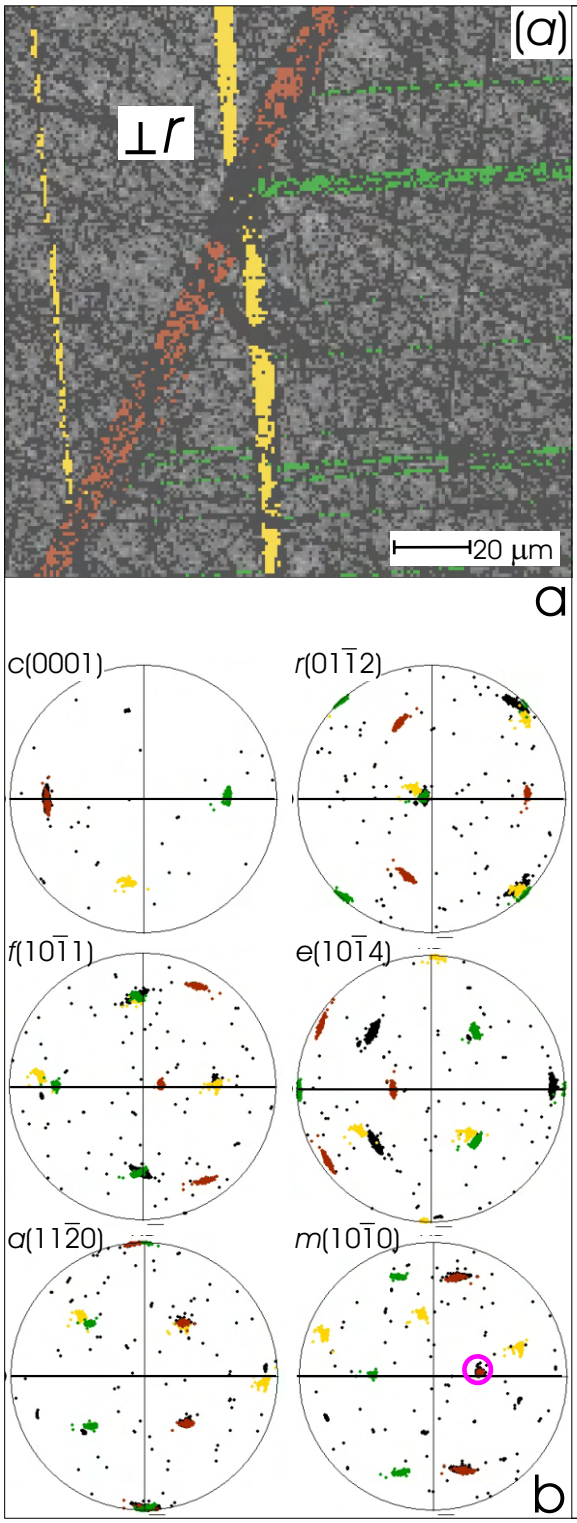
(a)
⊥r
20 µm
a
c(0001)
r(01$\bar{1}$2)
f(10$\bar{1}$1)
e(10$\bar{1}$4)
a(11$\bar{2}$0)
m(10$\bar{1}$0)
b

Fig. 11

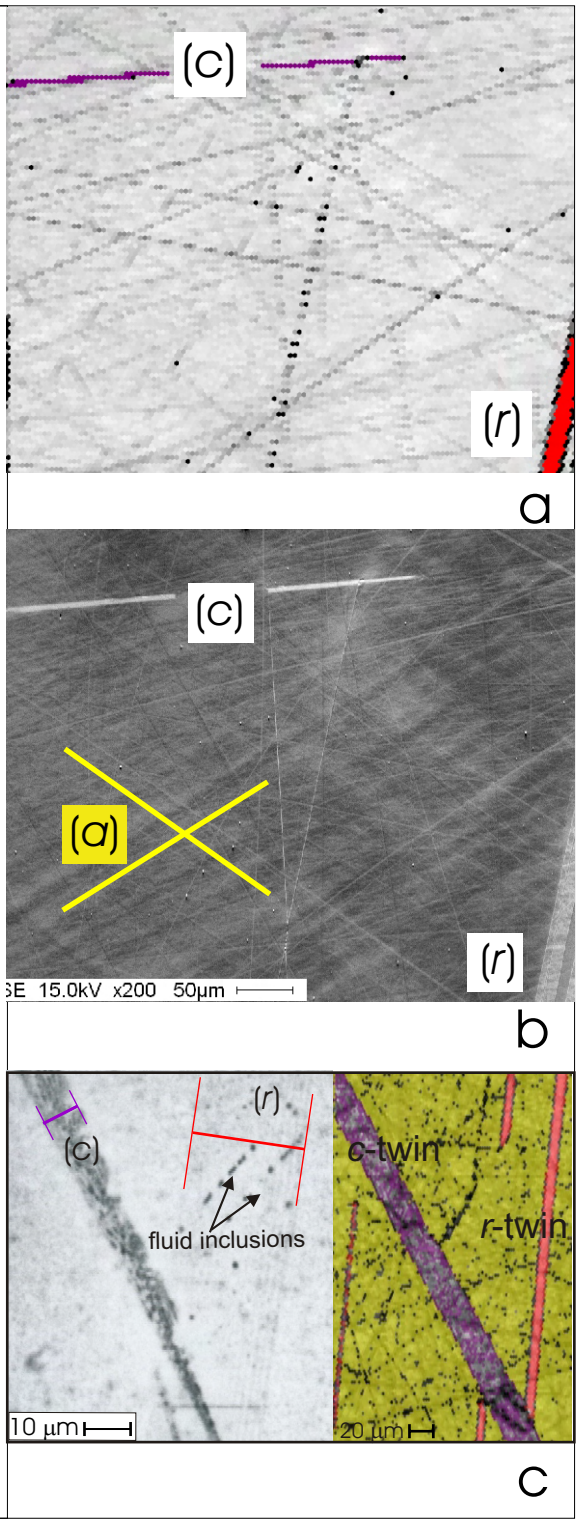
(c)
(r)
a
(c)
(a)
(r)
SE 15.0kV x200 50µm
b
(c)
(r)
fluid inclusions
c-twin
r-twin
10 µm
20 µm
c

Fig. 13

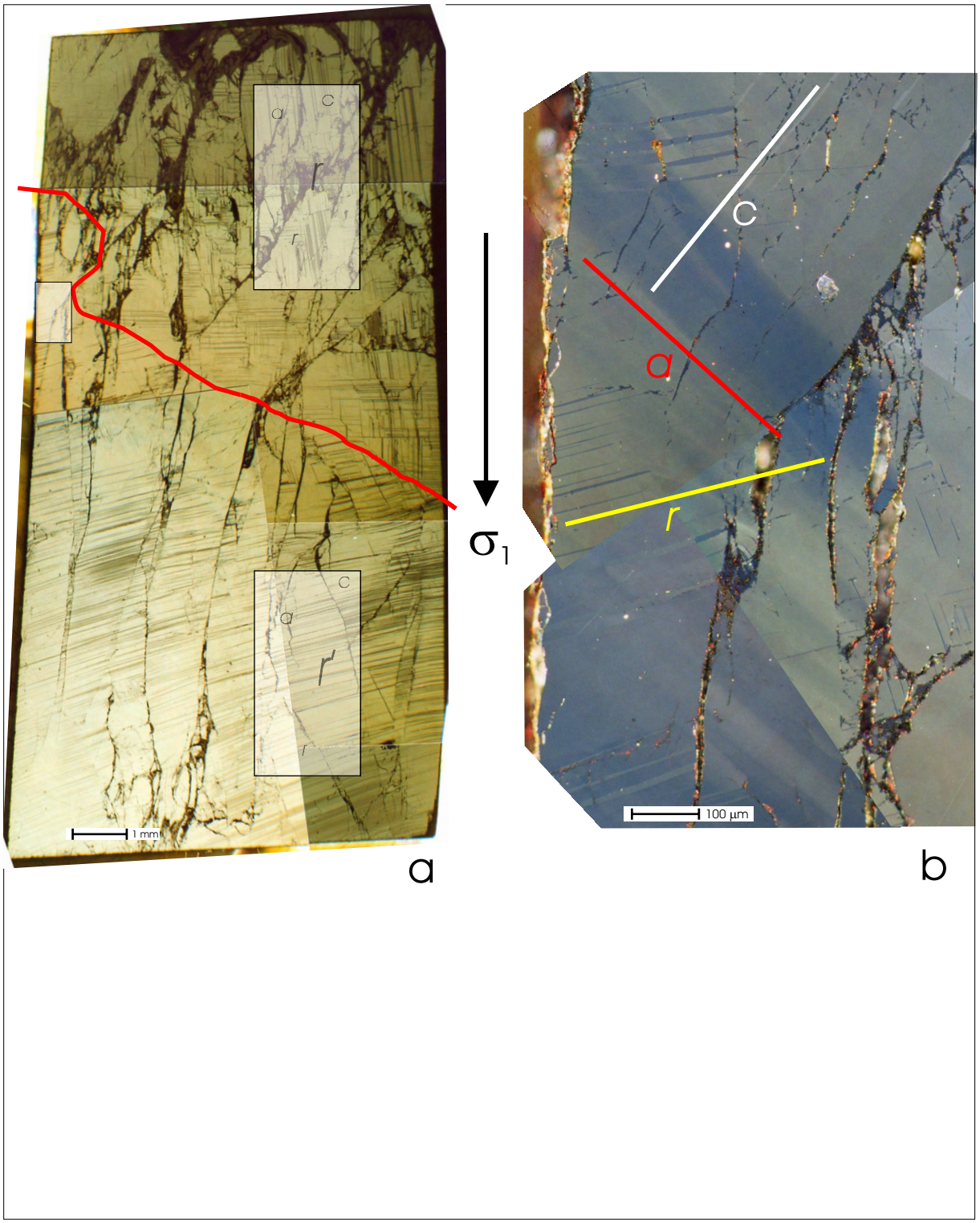

Fig. 12

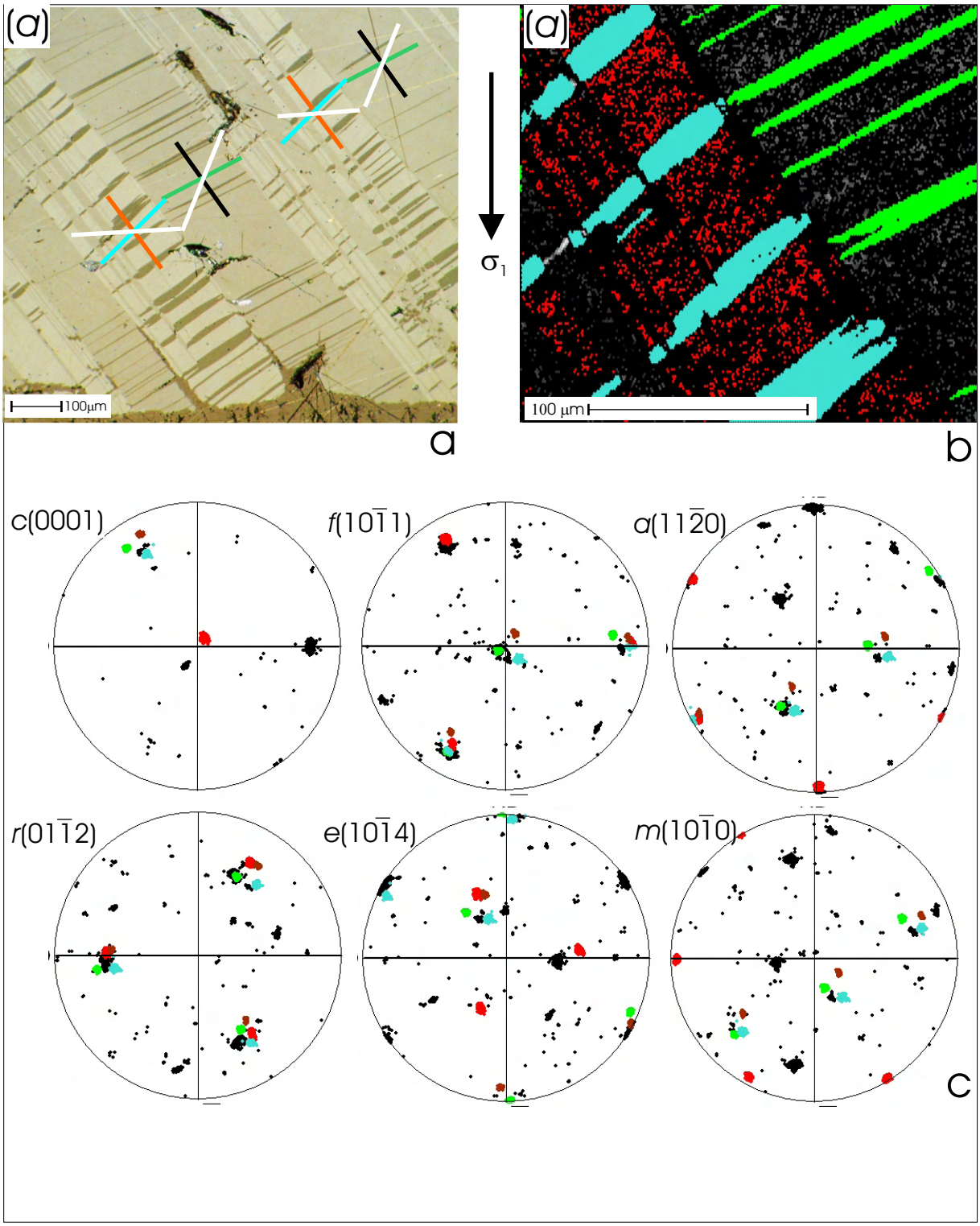
(a)
100μm
a
(a)
σ1
100 μm
b
c(0001)
f(10$\bar{1}$1)
a(11$\bar{2}$0)
r(01$\bar{1}$2)
e(10$\bar{1}$4)
m(10$\bar{1}$0)
c

Fig. 14

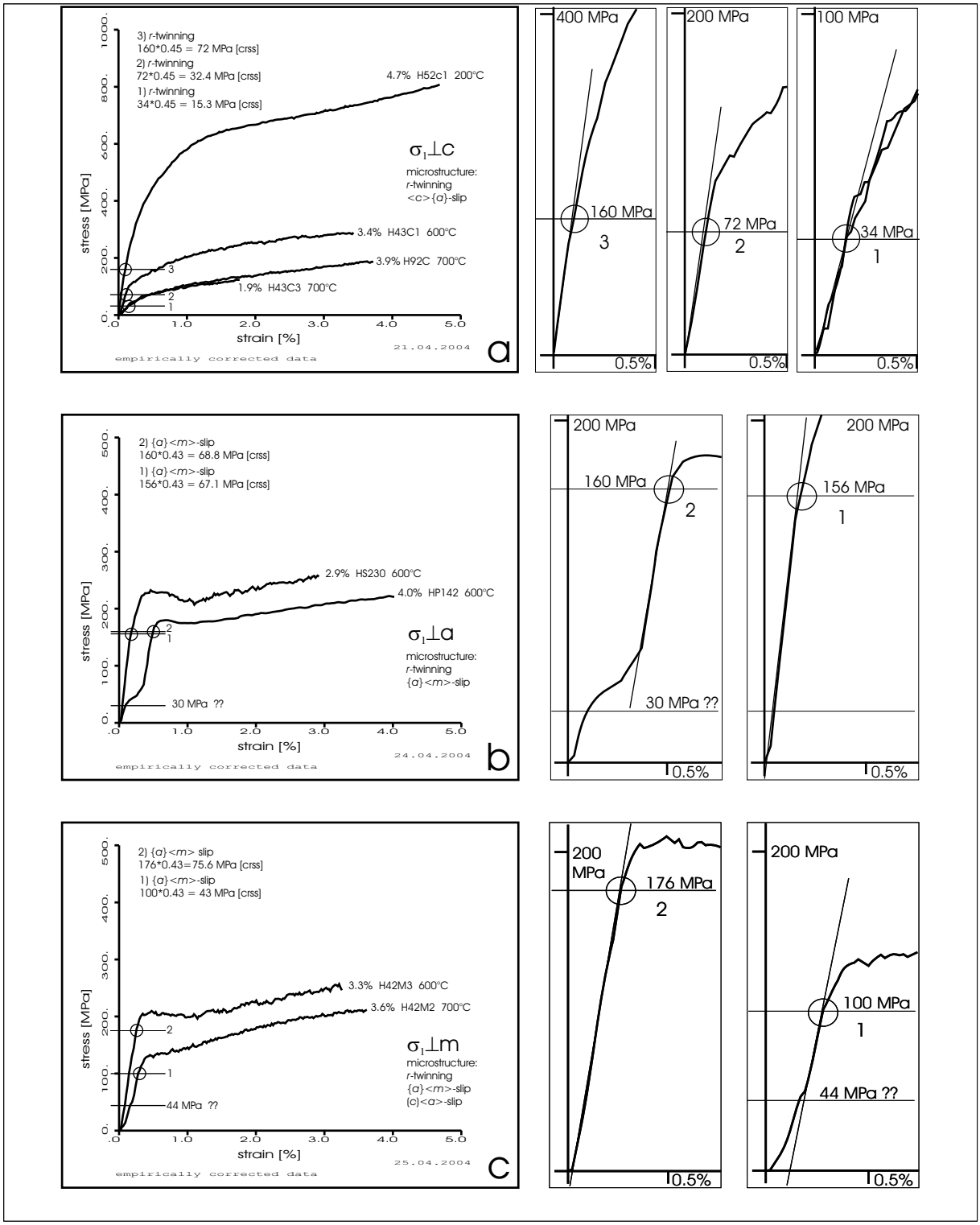
3) r-twinning
160*0.45 = 72 MPa [crss]
2) r-twinning
72*0.45 = 32.4 MPa [crss]
1) r-twinning
34*0.45 = 15.3 MPa [crss]
4.7% H52c1 200°C
σ1⊥c
microstructure:
r-twinning
<c>{a}-slip
3.4% H43C1 600°C
3.9% H92C 700°C
1.9% H43C3 700°C
stress [MPa]
strain [%]
empirically corrected data
21.04.2004
a
400 MPa
160 MPa
3
200 MPa
72 MPa
2
100 MPa
34 MPa
1
0.5%
2) {a}<m>-slip
160*0.43 = 68.8 MPa [crss]
1) {a}<m>-slip
156*0.43 = 67.1 MPa [crss]
2.9% HS230 600°C
4.0% HP142 600°C
σ1⊥a
microstructure:
r-twinning
{a}<m>-slip
30 MPa ??
24.04.2004
b
200 MPa
160 MPa
2
30 MPa ??
156 MPa
1
2) {a}<m> slip
176*0.43=75.6 MPa [crss]
1) {a}<m>-slip
100*0.43 = 43 MPa [crss]
3.3% H42M3 600°C
3.6% H42M2 700°C
σ1⊥m
microstructure:
r-twinning
{a}<m>-slip
(c)<a>-slip
44 MPa ??
25.04.2004
c
200 MPa
176 MPa
100 MPa
44 MPa ??

Fig. 15 a-c

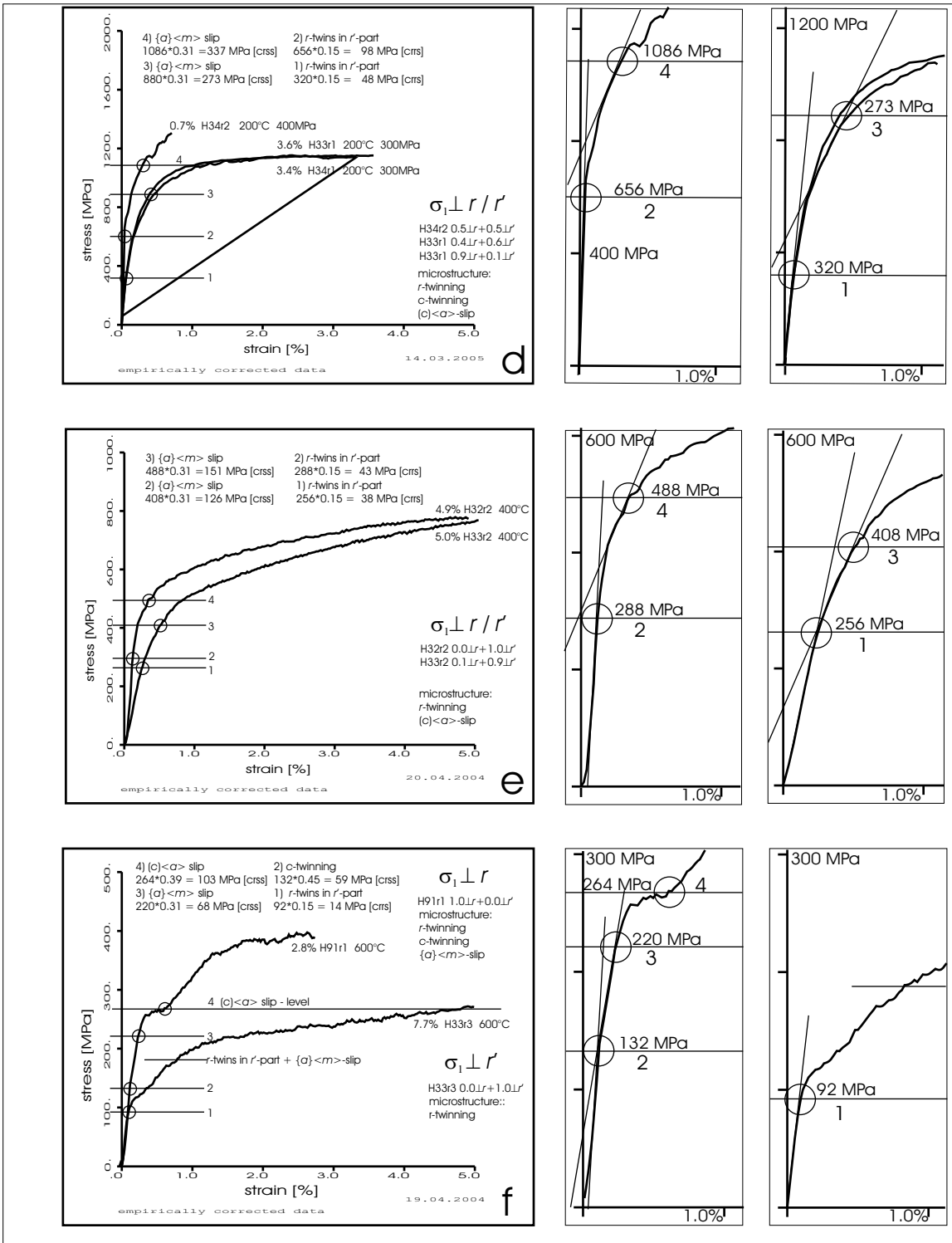
4) {a}<m> slip
1086*0.31 =337 MPa [crss]
3) {a}<m> slip
880*0.31 =273 MPa [crss]
2) r-twins in r'-part
656*0.15 = 98 MPa [crrs]
1) r-twins in r'-part
320*0.15 = 48 MPa [crrs]
0.7% H34r2 200°C 400MPa
3.6% H33r1 200°C 300MPa
3.4% H34r1 200°C 300MPa
σ1⊥ r / r'
H34r2 0.5⊥r+0.5⊥r'
H33r1 0.4⊥r+0.6⊥r'
H33r1 0.9⊥r+0.1⊥r'
microstructure:
r-twinning
c-twinning
(c)<a>-slip
stress [MPa]
strain [%]
empirically corrected data
14.03.2005
d
1086 MPa
656 MPa
400 MPa
1200 MPa
273 MPa
320 MPa
1.0%
3) {a}<m> slip
488*0.31 =151 MPa [crss]
2) {a}<m> slip
408*0.31 =126 MPa [crss]
2) r-twins in r'-part
288*0.15 = 43 MPa [crrs]
1) r-twins in r'-part
256*0.15 = 38 MPa [crrs]
4.9% H32r2 400°C
5.0% H33r2 400°C
σ1⊥ r / r'
H32r2 0.0⊥r+1.0⊥r'
H33r2 0.1⊥r+0.9⊥r'
microstructure:
r-twinning
(c)<a>-slip
20.04.2004
e
600 MPa
488 MPa
288 MPa
600 MPa
408 MPa
256 MPa
4) (c)<a> slip
264*0.39 = 103 MPa [crss]
3) {a}<m> slip
220*0.31 = 68 MPa [crss]
2) c-twinning
132*0.45 = 59 MPa [crss]
1) r-twins in r'-part
92*0.15 = 14 MPa [crrs]
σ1⊥ r
H91r1 1.0⊥r+0.0⊥r'
microstructure:
r-twinning
c-twinning
{a}<m>-slip
2.8% H91r1 600°C
4 (c)<a> slip - level
7.7% H33r3 600°C
r-twins in r'-part + {a}<m>-slip
σ1⊥ r'
H33r3 0.0⊥r+1.0⊥r'
microstructure::
r-twinning
19.04.2004
f
300 MPa
264 MPa
220 MPa
132 MPa
300 MPa
92 MPa

Fig. 15 d-f

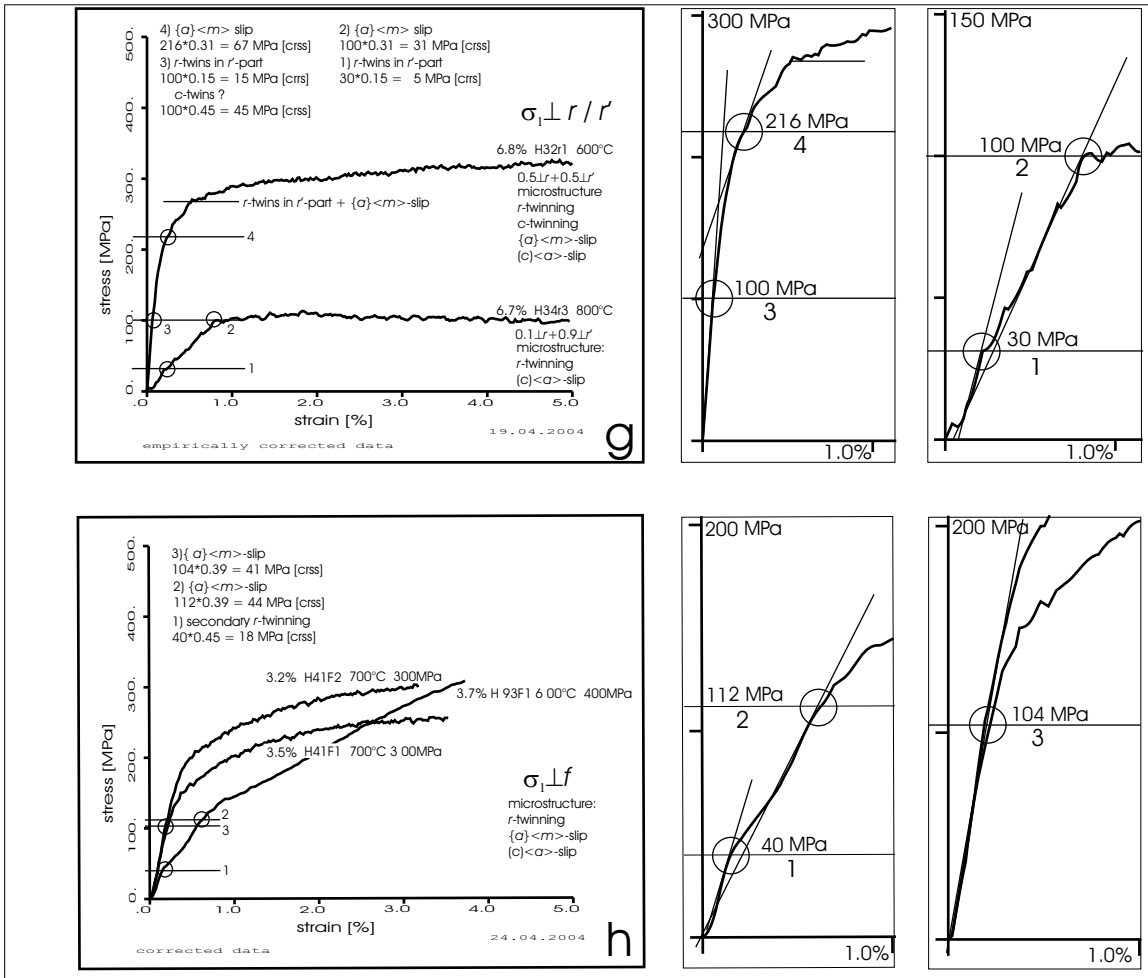
4) {a}<m> slip
216*0.31 = 67 MPa [crss]
3) r-twins in r'-part
100*0.15 = 15 MPa [crrs]
c-twins ?
100*0.45 = 45 MPa [crss]
2) {a}<m> slip
100*0.31 = 31 MPa [crss]
1) r-twins in r'-part
30*0.15 = 5 MPa [crrs]
σ1⊥ r / r'
6.8% H32r1 600°C
0.5⊥r+0.5⊥r'
microstructure
r-twinning
c-twinning
{a}<m>-slip
(c)<a>-slip
r-twins in r'-part + {a}<m>-slip
6.7% H34r3 800°C
0.1⊥r+0.9⊥r'
microstructure:
r-twinning
(c)<a>-slip
stress [MPa]
strain [%]
empirically corrected data
19.04.2004
g
300 MPa
216 MPa
4
100 MPa
3
1.0%
150 MPa
100 MPa
2
30 MPa
1
1.0%
3){ a}<m>-slip
104*0.39 = 41 MPa [crss]
2) {a}<m>-slip
112*0.39 = 44 MPa [crss]
1) secondary r-twinning
40*0.45 = 18 MPa [crss]
3.2% H41F2 700°C 300MPa
3.7% H 93F1 6 00°C 400MPa
3.5% H41F1 700°C 3 00MPa
σ1⊥f
microstructure:
r-twinning
{a}<m>-slip
(c)<a>-slip
stress [MPa]
strain [%]
corrected data
24.04.2004
h
200 MPa
112 MPa
2
40 MPa
1
1.0%
200 MPa
104 MPa
3
1.0%

Fig. 15 g-h

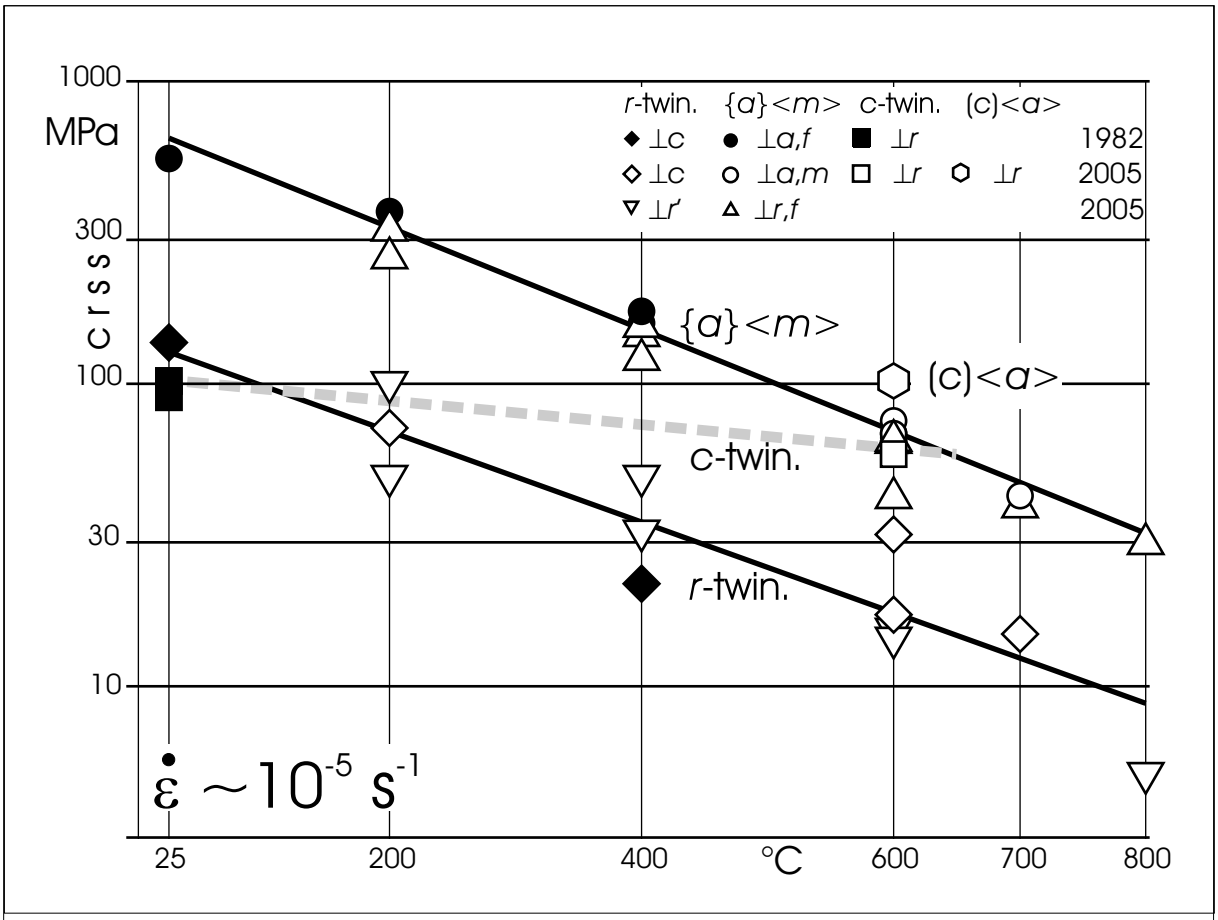
1000
MPa
300
crss
100
30
10
r-twin. {a}<m> c-twin. (c)<a>
⊥c ⊥a,f ⊥r 1982
⊥c ⊥a,m ⊥r ⊥r 2005
⊥r' ⊥r,f 2005
{a}<m>
(c)<a>
c-twin.
r-twin.
ε̇ ~10-5 s-1
25
200
400
°C
600
700
800

Fig. 16